



**HAL**  
open science

## Multifrequency seismic detectability of seasonal thermoclines assessed from ARGO data

Stephan Ker, Yves Le Gonidec, L. Marié

► **To cite this version:**

Stephan Ker, Yves Le Gonidec, L. Marié. Multifrequency seismic detectability of seasonal thermoclines assessed from ARGO data. *Journal of Geophysical Research. Oceans*, 2016, 121 (8), pp.6035-6060. 10.1002/2016JC011793 . insu-01355184

**HAL Id: insu-01355184**

**<https://insu.hal.science/insu-01355184>**

Submitted on 22 Aug 2016

**HAL** is a multi-disciplinary open access archive for the deposit and dissemination of scientific research documents, whether they are published or not. The documents may come from teaching and research institutions in France or abroad, or from public or private research centers.

L'archive ouverte pluridisciplinaire **HAL**, est destinée au dépôt et à la diffusion de documents scientifiques de niveau recherche, publiés ou non, émanant des établissements d'enseignement et de recherche français ou étrangers, des laboratoires publics ou privés.

## RESEARCH ARTICLE

10.1002/2016JC011793

## Multifrequency seismic detectability of seasonal thermoclines assessed from ARGO data

S. Ker<sup>1</sup>, Y. Le Gonidec<sup>2</sup>, and L. Marié<sup>3</sup>

<sup>1</sup>IFREMER, Géosciences marines, Centre de Brest, Plouzané, France, <sup>2</sup>Géosciences Rennes, Université Rennes 1, CNRS, Campus de Beaulieu, Rennes, France, <sup>3</sup>Laboratoire d'Océanographie Physique et Spatiale, UMR 6523, Univ. Brest/CNRS/IFREMER/IRD, Brest, France

## Key Points:

- The seismic reflectivity of seasonal thermoclines is quantified for a large data set of hydrographic profiles for frequencies (50–1000 Hz)
- We provide the first probability distribution of multifrequency seismic amplitudes of thermocline reflectors for the Armorican Shelf
- Optimal seismic detectability of shallow thermoclines requires multichannel seismic experiments with peak frequencies in 200–400 Hz

## Correspondence to:

S. Ker,  
stephan.ker@ifremer.fr

## Citation:

Ker, S., Y. Le Gonidec, and L. Marié (2016), Multifrequency seismic detectability of seasonal thermoclines assessed from ARGO data, *J. Geophys. Res. Oceans*, 121, doi:10.1002/2016JC011793.

Received 11 MAR 2016

Accepted 24 JUL 2016

Accepted article online 2 AUG 2016

**Abstract** Seismic oceanography is a developing research topic where new acoustic methods allow high-resolution teledetection of the thermohaline structure of the ocean. First implementations to study the Ocean Surface Boundary Layer have recently been achieved but remain very challenging due to the weakness and shallowness of such seismic reflectors. In this article, we develop a multifrequency seismic analysis of hydrographic data sets collected in a seasonally stratified midlatitude shelf by ARGO network floats to assess the detectability issue of shallow thermoclines. This analysis, for which sensitivity to the data reduction scheme used by ARGO floats for the transmission of the profiles is discussed, allows characterizing both the depth location and the frequency dependency of the dominant reflective feature of such complex structures. This approach provides the first statistical distribution of the range of variability of the frequency-dependent seismic reflection amplitude of the midlatitude seasonal thermoclines. We introduce a new parameter to quantify the overall capability of a multichannel seismic setup, including the source strength, the fold, and the ambient noise level, to detect shallow thermoclines. Seismic source signals are approximated by Ricker wavelets, providing quantitative guidelines to help in the design of seismic experiments targeting such oceanic reflectors. For shallow midlatitude seasonal thermoclines, we show that the detectability is optimal for seismic peak frequencies between 200 and 400 Hz: this means that airgun and Sparker sources are not well suited and that significant improvements of source devices will be necessary before seismic imaging of OSBL structures can be reliably attempted.

## 1. Introduction

Our capability to understand the climate system and predict its evolution depends, in a critical way, on our understanding of the way the upper ocean assimilates, disperses, or rejects thermohaline anomalies forced by its interaction with the atmosphere [Ferrari, 2011]. Observing the thermohaline structure of the Ocean Surface Boundary Layer (OSBL) at adequate resolutions remains unfortunately extremely challenging from an experimental point of view. Traditional methods employ a material sensor which is swept across the water column either vertically (standard CTD or expendable probes casts, microstructure sensors), horizontally (towed thermistor chains), or in a see-saw pattern (SeaSoar, Scanfish, etc. . .). Profile methods can provide very high resolutions of few centimeters in the vertical, but are restricted in the horizontal by the time required to acquire each individual profile. Towed thermistor chains can provide very high resolution of few meters in the horizontal, but are necessarily restricted in the vertical by the affordable number of probes and the hydrodynamic drag on the tow cable. Towed undulating instruments [Brown *et al.*, 1996], finally, provide a trade-off between the two but are restricted to profile slopes of order 0.25 at most, yielding horizontal resolutions of one complete cycle every eight profiling depths. In the meantime, modeling studies unveil the importance of eddies of ever-smaller horizontal scales [Boccaletti *et al.*, 2007; Lévy *et al.*, 2010; Ponté *et al.*, 2013; Gula *et al.*, 2015] on surface-layer dynamics.

It seems therefore that a teledetection technique capable of observing the thermohaline structure of the upper ocean at consistent horizontal and vertical resolutions on the order of a few meters would be most needed: “seismic oceanography,” namely multichannel seismic (MCS) reflection imagery of oceanographic structures, has been developed and is now an established technique for the teledetection of the thermohaline structure of the inner ocean, allowing to study with horizontal and vertical resolutions of the order of 10 m structures several hundred kilometers in length, such as eddies [Biescas *et al.*, 2008; Ménesquen *et al.*, 2012],

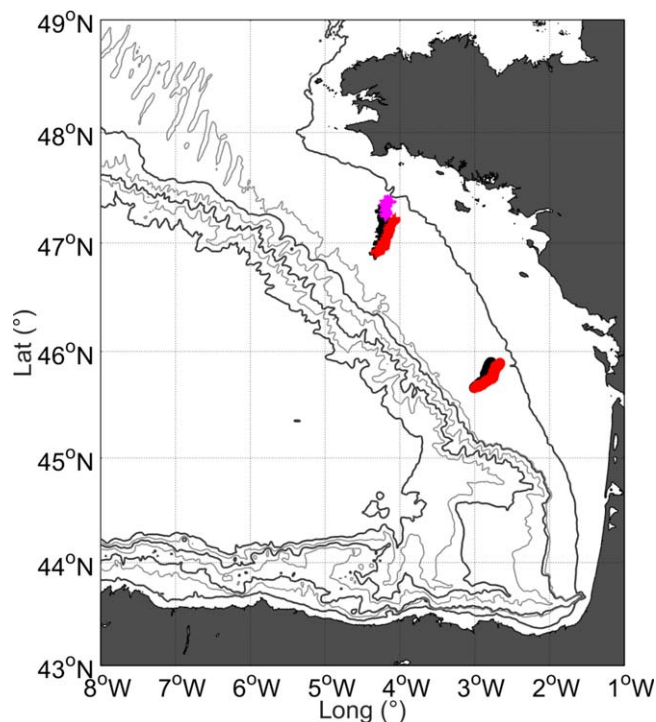


**Figure 1.** Location map of the five ARGO data sets: two sites, North and South (+, °, respectively) and three deployment years, 2011, 2012, and 2014 (black and red, respectively, for the LR data set, magenta for the HR data set). The northern deployment site location is 46°54'N, 4°20'W, and the southern deployment site location is 45°40'N, 3°W. Starting from the coast, the grey lines mark the 100, 150, 200, 1000, 2000, 3000, 4000 m isobaths.

current flows [Mirshak *et al.*, 2010], internal gravity waves [Holbrook and Fer, 2005; Holbrook *et al.*, 2009], thermohaline intrusions [Holbrook *et al.*, 2003], and thermohaline staircases [Buffet *et al.*, 2009; Biescas *et al.*, 2010; Fer *et al.*, 2010].

But seismic imaging of shallow mixed layers remain rare in the literature [Piété *et al.*, 2013; Sallarès *et al.*, 2016]: [Piété *et al.*, 2013] reports a successful attempt at using the teledetection technique to observe a shallow structure, the seasonal thermocline of the Armorican Shelf, on the western margins of France, and discusses the specific challenges of designing a seismic experiment targeting shallow water structures. To the knowledge of the present authors, this successful implementation of seismic oceanography in a shallow environment remains sole of its kind. Several months later, indeed, the same setup, though marginally improved and operated by the same team, failed to observe the same structure, in the same area [Thomas *et al.*, 2013]. The study by Ker *et al.* [2015] explains these different outcomes by providing a multiscale

seismic analysis of the temperature profiles encountered during the two cruises, and showing that seemingly minor differences in the profiles lead to strongly different seismic responses: however, for want of a large enough set of temperature profiles, this recent work left open the question of the variability of the seismic reflectivity of the seasonal thermocline in response to natural sources of variability such as internal gravity waves, mixing events due to atmospheric forcing, or the seasonal cycle of stratification/destratification.

The present contribution is aimed at filling this gap, by taking advantage of a large set of temperature/salinity profiles collected daily over 2 years and at two different sites on the Armorican Shelf by profiling floats from the ARGO program to study the probability distribution of the seismic reflectivity of a “benchmark” structure, in response to natural variability sources. The geographical setting and the two data sets used in this study are described in section 2: the first one comprises 106 temperature/salinity profiles at 30 cm depth resolution and the second one comprises 892 profiles, but at the coarser depth resolution of 1 m. In section 3, we introduce the basic principles of the multiscale seismic analysis method used to characterize the dominant seismic reflector of a shallow oceanic structure and to define its depth location. In section 4, we apply this wavelet-based method to the high-resolution data set in the frequency range 50–1000 Hz to estimate the average frequency dependency of the seismic reflection amplitudes: we also assess the impact of the profile resolution on the quantitative results, then extend our analysis using the more comprehensive data set of lower-resolution temperature profiles. We provide a characterization of the probability distribution function of the multiscale seismic response of the seasonal thermocline on the Armorican shelf. Sections 5 and 6 are dedicated to the detectability issue: in the former, we introduce a new parameter to quantify the capability of a seismic experiment to detect thermoclines and give some insights on how quantifying this parameter in order to discuss the conditions of thermocline detectability. In the latter, we develop the detectability issue for the seasonal thermoclines of the Armorican Shelf using Ricker source wavelets. We finally draw some conclusions and propose new guidelines for the design of seismic experiments targeting shallow oceanographic structures.

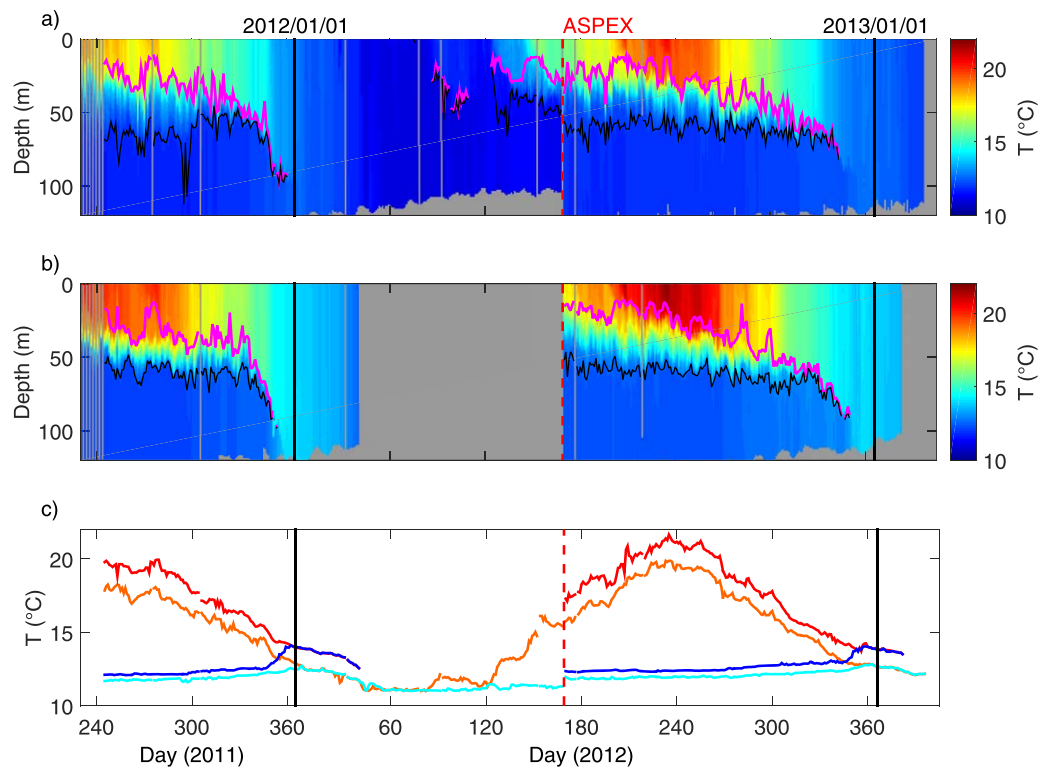


**Figure 2.** Temperature profiles of the LR data set collected respectively at the (a) north and (b) south sites: the thin magenta and black lines mark, respectively, the bottom of the surface mixed layer and the top of the bottom mixed layer. (c) Temperature time series at 10 m depth at the north (orange) and south (red) sites, and at the seafloor at the north (cyan) and south (blue) sites. The vertical thick lines mark 1 January 2012 and 1 January 2013 (black) and the day of the ASPEX 2012 cruise (dashed red).

## 2. Description of the Hydrographic Data Sets

### 2.1. Geographical Location

The hydrographic measurements we analyze in the present work have been collected by the use of ARVOR-C profilers [André *et al.*, 2010] deployed as part of the ARGO network [Riser *et al.*, 2016] at two locations of the open waters of the Armorican Shelf, west of France (Figure 1). The main features of the hydrographical environment of the Armorican Shelf have been quite well described in previous studies [Vincent, 1973; Koutsikopoulos and Le Cann, 1996; Reverdin *et al.*, 2013]. In this characteristic midlatitude shelf sea environment, a very weak subtidal circulation exists except close to the shore and the shelf break [Charria *et al.*, 2013; Batifoulier *et al.*, 2013; Le Boyer *et al.*, 2013; Kersalé *et al.*, 2016], and the water column structure on the midshelf is governed by essentially 1-dimensional processes.

As clearly apparent in Figure 2, surface cooling and increased turbulent fluxes due to more frequent synoptic storm systems effectively mix the water column in winter, while increased solar fluxes and comparatively mild weather induce a seasonal stratification in summer [Vincent, 1973]. Topographic conversion of the large barotropic tide at the shelf break is the source of energetic internal tides and internal waves in summer [Pingree and New, 1995], which induce the day-to-day heave in seasonal thermocline depth apparent in Figure 2: this signal is aliased by the 1 day profiling period of the floats [Piété *et al.*, 2013]. The free-drifting profiling floats, or profilers, are recovered before they drift to the inshore zone where mixing due to internal tide dissipation is expected to affect significantly the water column structure. Finally, though in summer the surface layer waters are usually found to be fresher than the waters from the “Cold Pool” below, and though freshwater signatures from the Gironde and Loire river plumes have sometimes been observed quite far from the outlets of these rivers [Puillat *et al.*, 2004; Reverdin *et al.*, 2013], salinity is usually considered to have a much lesser dynamical influence than temperature, except maybe in short transitional periods in spring, where it could possibly play a role as a preconditioning agent of the thermal stratification inception.

Overall, the 998 profiles comprised in the data set (see section 2.2 below) sample a large panel of conditions typical of a midlatitude upper water column subject to a seasonal cycle of stratification/destratification. The location of the profilers on the shelf, while it simplifies considerably the logistics and permits fine depth and time resolution observations, has a minor influence on the statistical characteristics of the seismic reflectivity of the water column at seasonal thermocline depth during the summer period. Moreover, the distance between the two profiler deployment sites being small compared to typical atmospheric coherence lengths, it is probably a fairly good assumption to consider that the sets of floats deployed at the two points provide two realizations of essentially the same process.

## 2.2. ARVOR-C CTD Measurements

The data collection cycle of the ARVOR-C profiling floats is similar to the standard ARGO network measurement cycle, with minor modifications to better suit their continental-shelf environments:

1. Between profiles, the floats cling on the seafloor using stainless steel “claws,” fitted to their buoyancy bladder housings to reduce their drift.
2. During profiling, the CTD data are acquired at the raw frequency of 0.5 Hz, using a standard SBE41-CP sensor package: this 2 s sampling interval translates to a raw depth sampling interval comprised between 30 and 40 cm, depending on the floats rising speed.
3. At the surface, a data-reduction routine averages the raw CTD data in 1 dbar bins, i.e., roughly a 1 m depth sampling in order to transmit the data using the Iridium satellite communication system: each 1 dbar bin in the transmitted profiles thus represents the average of two, or three, raw data samples.
4. Upon completion of the data transmission, the floats dive again to the seafloor.

The time needed to complete a whole acquisition cycle is about 5 min for a deployment at 120 m water depth. Several features of these free-drifting floats make their data particularly well suited to the purposes of the present study:

1. For a variety of reasons (fishing activity, biological fouling of the sensors, overall coastward drift due to wind, and tidal currents), the floats need to be recovered, refitted, and redeployed every year: this short expected mission duration alleviates considerably energy constraints, allowing the floats to cycle once per day.
2. Due to the comparably shallow environment (profile depths range from 90 to 120 m as the floats drift coastward), data transmission issues are also strongly alleviated, making resolution loss, induced by data reduction prior to transmission, less drastic: CTD data only need to be averaged on a 1 dbar depth grid, compared to the 10 dbar or even coarser grids used by most of the standard floats of the ARGO network [Riser *et al.*, 2016].
3. Finally, the fact that the floats are recovered at the end of each year allows, in some instances, retrieving the raw 0.5 Hz CTD data stored in their buffer memories: though these data represent only a fraction of the total number of profiles, they permit an interesting analysis of the impact of the data reduction scheme on the suitability of the ARGO network data for seismic oceanographic survey planning.

For the sake of brevity, we will refer in the following to the set of CTD profiles retrieved from the buffer memory on recovery of the profilers as the “High-Resolution” data set, and to the set of profiles collected using the standard Iridium transmission chain as the “Low-Resolution” data set. However, it is important to note that its resolution is actually finer by an order of magnitude than that of usual ARGO network data.

## 2.3. High-Resolution CTD Data Set

The “High Resolution” (HR) CTD data set is composed of 106 hydrographic profiles acquired in 2015 between days 76 and 181 by Argo float 6901681, deployed in 2014 at the northern deployment site of the Armorican Shelf (Figure 1, see also Table 1). For this data set, salinity (expressed according to the 1978 practical salinity scale) is limited to the range 35.4–35.45. Temperature spans the range 11–18°C, and the seasonal thermocline is shallow, remaining limited to the range 10–100 m of water depth. The CTD data have been retrieved directly from the internal memory card of the float, with an irregular depth sampling interval comprised in the pressure range 0.3–0.4 dbar: for the present study, the data have been interpolated (b-spline algorithm) to a regular grid with a depth sampling interval of 30 cm.

These data are similar in quality and resolution to the SBE-25 CTD casts used in [Piété *et al.*, 2013] and [Ker *et al.*, 2015] to discuss the contrasting seismic reflectivities of the Armorican Shelf seasonal thermocline

**Table 1.** Description of the Hydrographic Data Sets Collected on the Armorican Shelf by ARGO Network Floats: in the Text, the First and Second Data Sets Correspond to the High-Resolution (106 HR Profiles) and Low-Resolution (892 LR Profiles) Measurements, Respectively

Deployment year	Site	WMO Number	Date of First Profile	Date of Last Profile	Number of Profiles	Depth Sampling
2014	North	6901681	17 Mar 2015	30 Jun 2015	106	30 cm (HR)
2012	North	6901421	18 Jun 2012	30 Jan 2013	225	1 m (LR)
	South	6901420	18 Jun 2012	16 Jan 2013	211	1 m (LR)
2011	North	6900962	19 Aug 2011	17 Jun 2012	290	1 m (LR)
	South	6900963	19 Aug 2011	9 Feb 2012	166	1 m (LR)

encountered during the ASPEX and IFOSISMO cruises of 2012. *Ker et al.* [2015] quantified the multifrequency seismic response of these two particular thermocline structures but the ASPEX case remains the only instance of thermocline detection by a very high-resolution seismic experiment: one of the key objectives of this work is to consider the ASPEX CTD profile in the context of a larger set of HR profiles, to assess the issue of seasonal thermocline detectability in a broader context.

In addition to being retrieved from the float at recovery, the profiles comprising the HR data set were also collected in the usual way using Iridium communications, i.e., after data averaging to 1 dbar bins: this means that the data set is available at both the high and low resolutions studied in this work. This original data redundancy is interesting for two objectives. First, we can reduce the HR data set to the LR resolution in order to check the sensitivity of our results to the data reduction method implemented in the ARGO floats. Second, and most importantly for the present study, we can use these two data sets to quantify the impact of the depth sampling resolution on the multiscale seismic analysis results: the method has been used by *Ker et al.* [2015] on the ASPEX and IFOSISMO high-resolution CTD profiles, but most of the ARGO hydrographic data are available only at the low resolution, which thus deserves to be studied in detail.

#### 2.4. Low-Resolution CTD Data Set

The “Low Resolution” (LR) CTD data set is a much larger data set: it is composed of 892 individual profiles, collected using the usual ARGO data transmission chain, i.e., with a depth sampling interval of 1 m. The profiles were collected by floats deployed at both sites (Figure 1) and correspond to four subdata sets comprising data acquired at both sites in 2011 and 2012 (Table 1).

The observed salinity values (not shown) show little variability over the whole LR data set, ranging mainly between 35.4 and 35.75. When a seasonal stratification is present, salinity contrasts tend to mirror temperature variations, water tending to be fresher and warmer above the thermocline than below. Gradients of salinity and temperature thus tend to be tightly collocated in the vertical. In some instances in spring, increased run-offs of the Loire and the Gironde lead these river plumes to encroach over the shelf to the floats locations, and some glimpses of haline stratification can be observed. While dynamically significant as preconditioning factors of the thermal stratification inception, we will see in the following that these salinity gradients are too slight to induce significant seismic reflection, and these events remain inconsequential to the results of this study.

In contrary, strong fluctuations of the temperature parameter are observed both across the water column and during the year (Figure 2): while the short-term fluctuations, which reflect the influence of synoptic weather events, are highly irregular, the evolution on seasonal time scales is very similar for the four subdata sets, i.e., for both sites and both years of measurements, and displays the basic known features discussed in section 2.1:

1. From the end of spring to the end of autumn, a seasonal thermocline located between depths 20 and 50 m separates the upper and lower parts of the water column.
2. Thermal exchanges between atmosphere and the ocean involve only the upper part of the water column, where temperature fluctuates, but is kept mixed in the vertical by synoptic weather events.
3. The body of cool water located under the thermocline remains at a nearly constant temperature of 12°C.
4. Over fall and the beginning of winter, the thermocline deepens until it encounters the seafloor: from then on, the water column temperature varies uniformly, in response to surface heat fluxes, and in that respect, our observations differ from what would be observed over the abyssal plain nearby [*Somavilla et al.*, 2013].

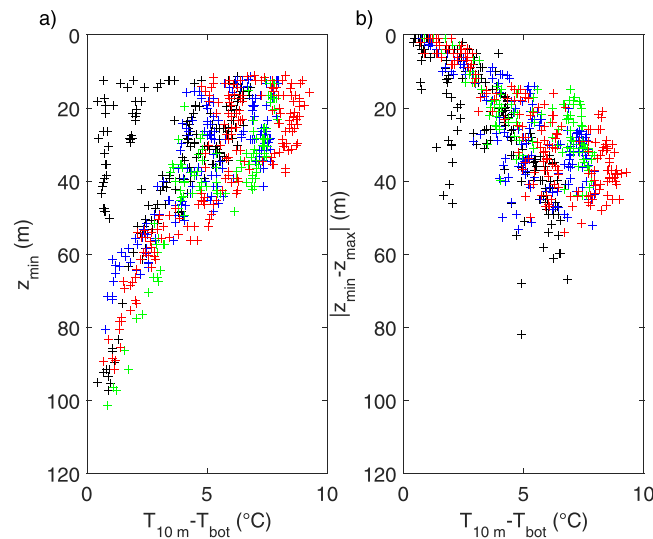


**Figure 3.** Parameters measured from the profiles of the LR data set which featured thermoclines: (a) crossplot between the temperature contrast across the thermocline and the thermocline depth  $z_{min}$ . (b) crossplot between the temperature contrast across the thermocline and the thermocline thickness  $\Delta z$ . Black (+): North site, 2011 deployment. Blue (+): North site, 2012 deployment. Green (+): South site, 2011 deployment. Red (+): South site, 2012 deployment.

Due to the mixing events occurring in the surface mixed layer, and the continuous stretching and straining motion caused by internal gravity waves, the fine structure of the seasonal thermocline changes permanently on rapid time scales. The motivation of the present study is to assess in what respect these constant fine structure changes affect the seismic detectability of the seasonal thermocline, and in what respect seismic oceanography might be useful to study these processes.

### 2.5. Seasonal Thermocline Properties

As a first approximation, we characterize the vertical geometry of a thermocline structure by two main parameters: (i) the depth  $z_{min}$  of the base of the surface mixed layer, which can be identified by the main discontinuity of the temperature profile, i.e.,

the dominant contrast of the thermohaline properties, and (ii) the thickness  $\Delta z = |z_{max} - z_{min}|$  of the large-scale structure of the thermocline. The depths  $z_{min}$  and  $z_{max}$  correspond to the upper and lower boundaries of the thermocline structure, respectively, but their definition is not straightforward.

Actually, *de Boyer-Montégut et al.* [2004] defined  $z_{min}$  by the first point where the temperature is lower by  $0.2^\circ\text{C}$  than at the reference depth of 10 m. However, this definition cannot be applied in the present study which deals with many different morphologies of thermocline structures and is thus replaced by the following: when the top layer temperature is nearly constant, we define  $z_{min}$  as the depth where the temperature first drops by  $0.1^\circ\text{C}$ , otherwise where the temperature gradient first rises by  $-0.2^\circ\text{C}/\text{m}$ . As shown in *Johnston and Rudnick, 2009*, the converse problem of defining the base of the thermocline is more intricate, and has not received a well-accepted solution up to now. As a practical definition, we have chosen to use for this purpose the top of the bottom mixed layer, i.e., the depth  $z_{max}$ , defined as the first immersion where temperature is  $0.05^\circ\text{C}$  higher than at the seafloor. While this is convenient in the two layers-like setting studied in this work, such a definition could not apply in the open ocean, or for too complex thermocline structures.

We have represented  $z_{min}$ ,  $z_{max}$ , and the temperatures at the surface and bottom for the four deployments of the LR data set in Figures 2a, 2b, and 2c. It is quite clear that the processes occurring at the north and south sites for the 2 years are very similar: the seasonal thermocline depths are similar in all four cases, and their evolutions and disappearance in fall and winter are similar. Unfortunately, due to technical issues, only one occurrence of thermocline inception could be observed, at the north site in spring 2012. The time evolution of 10 m and bottom temperatures ( $T_{10\text{ m}}$  and  $T_{bot}$ , respectively) are also similar for all four deployments, the temperatures at the south site being higher by roughly one degree from those at the north site. In all cases, it is also quite clear that bottom temperatures evolve only very slowly over the stratified period, and that the temperature contrast across the thermocline essentially follows the evolutions of the surface temperature.

We have represented in Figure 3 scatter plots of the thermocline depth  $z_{min}$  and thickness  $\Delta z$  as functions of the temperature contrast across the thermocline  $T_{10\text{ m}} - T_{bot}$ : the sets of points corresponding to the four deployments strongly overlap, showing that statistical analyses performed on the compound data set are indeed meaningful. The temperature contrast and thermocline depths and thicknesses are strongly correlated, strong (summer) thermoclines being usually higher in the water column and more diffuse than weak ones. Care must be taken when interpreting these graphs that most of the variations they display actually

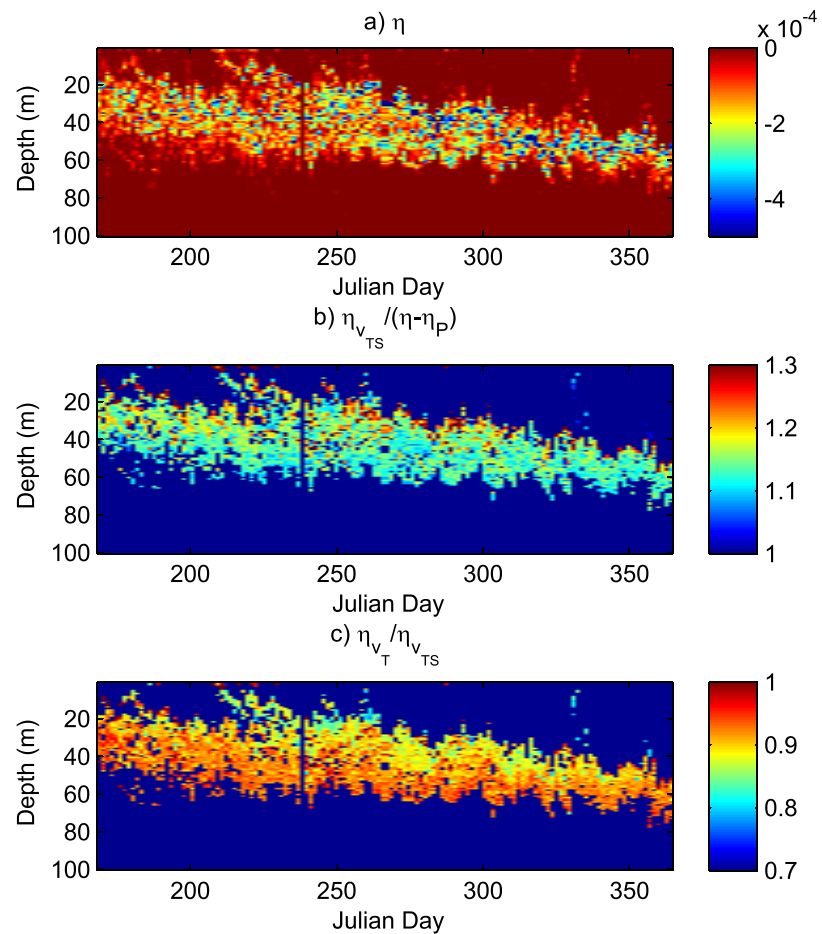


**Figure 4.** Reflectivity values estimated from the temperature profiles acquired in 2012 at the South site (a) when the hydrographic parameters T, S, and P are all taken into account; (b) contribution of the sound velocity contribution  $\eta_{VTS}$  when the pressure contribution is removed from the global reflectivity  $\eta$ ; and (c) ratio of the temperature contribution to the whole sound velocity contribution  $\eta_{VT}/\eta_{VTS}$ .

correspond to the fall deepening of the thermocline. The tendency of thermoclines to deepen and thin when they weaken is in fact the reflection of their fall and early winter behavior, apparent in Figure 2. The set of points corresponding to the spring 2012 thermocline inception appears distinctly out of the main cloud, on the left-hand side of the graphs, showing that the early summer behavior is probably different, but that our data set is still insufficient to describe it.

### 3. Multiscale Seismic Response: Identification of the Dominant Thermocline Features

#### 3.1. From Hydrographic Properties to Thermocline Seismic Reflectivity

A seismic reflection experiment consists in sounding the water column with an acoustic signal generated by a seismic source. The water column property relevant to the reflection of acoustic wave is the acoustic impedance profile  $\gamma(z) = v(z)\rho(z)$ , where  $v$  and  $\rho$  stand for the sound velocity and the density, respectively, functions of the water depth  $z$ . Based on the equation of state of seawater [Millero *et al.*, 1980],  $\rho$  and  $v$  both depend on the hydrographic parameters T (temperature), S (salinity), and P (pressure). Acoustic back-reflected waves are generated at each impedance contrast in the water column, which can thus be characterized by a profile of seismic reflectivity  $\eta(t) = \partial_t \log \gamma$ , where  $t$  is the two-way travel time between the transmitter and the receiver in normal incidence illumination.

The relative contributions of T, S, and P on the seismic reflectivity have been discussed in previous works [Ruddick *et al.*, 2009; Sallarès *et al.*, 2009] for mesoscale thermohaline structures such as meddies, in which

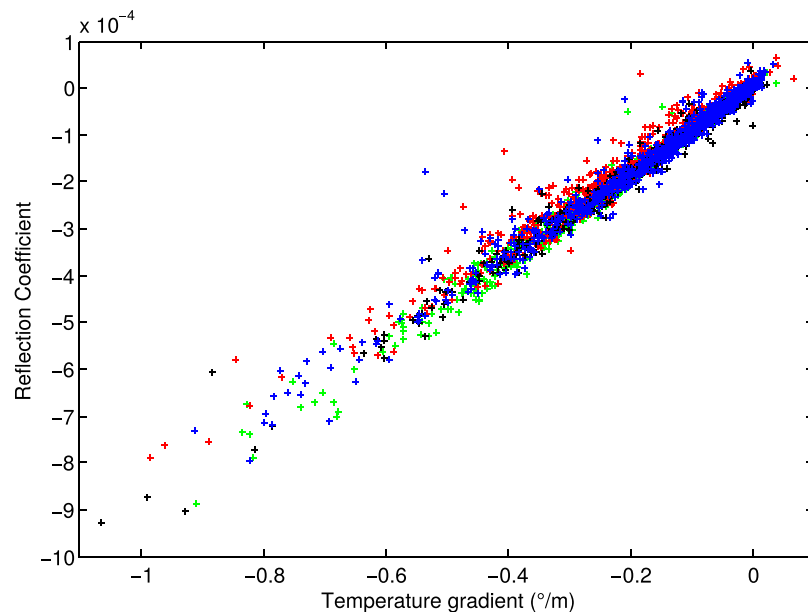


**Figure 5.** Reflection coefficient values plotted as a function of the temperature gradient for the four LR subdata sets. Symbols as in Figure 3.

gradients of the different hydrographic properties are typically distributed along several tens of meters in the vertical: taking benefits of our large LR hydrographic data set, we pursue this study in quantifying the parameters which contribute to the seismic reflectivity of sharper structures such as seasonal thermoclines. Because of the weak variations of both  $\rho$  and  $v$  observed in the whole LR data set, we approximate  $\eta = (\partial_z v / 2v) + (\partial_z \rho / 2\rho)$ , i.e., a linearized expression with two contributions  $\eta_{v(T,S,P)}$  and  $\eta_{\rho(T,S,P)}$ , respectively [Sallarès *et al.*, 2009]. Moreover, variations of  $\rho$  and  $v$  with respect to  $P$  are almost linear and thus  $\eta = \eta_{v(T,S)} + \eta_{\rho(T,S)} + \eta_P$

As an example, Figure 4a shows the computed values of  $\eta$  for the float deployed in 2012 at the southern site. Since  $\eta_{v(T,S)} > \eta - \eta_P$  for all the hydrographic profiles (Figure 4b),  $\eta$  is mainly controlled by fluctuations of  $v$  with depth. Figure 4c shows the relative share of the temperature-related variations of sound velocity in the total sound velocity-related reflectivity. Clearly, temperature variations are responsible for more than 90% of acoustic reflectivity, even in our shelf-sea situation where vertical salinity gradients can be considered strong with respect to usual open-ocean values.

As a consequence, we highlight that the seismic reflectivity  $\eta$  of sharp, shallow, thermohaline structures is mainly dominated by temperature variations along the water column, even in cases where unusually large salinity gradients are present. This result is supported by the whole hydrographic data sets acquired at the two different sites and years, composed of 892 profiles as described in section 2.4. Finally, when plotting the reflection coefficient calculated versus temperature gradient for all profiles, we clearly highlight a strong linear dependency, with a correlation better than 0.85 (Figure 5). This nice correlation strengthens analogous results on deep and large structures such as meddies, described by Ruddick *et al.* [2009] for instance, which emphasize that seismic images of the water column are in fact images of the temperature gradient. Our work demonstrates that these previous results can also be extended to shallower water structures.

### 3.2. Basic Principles of the Multiscale Seismic Response Study

The analysis introduced above deals with the seismic reflectivity sequence of the thermocline profile, as if the seismic source were an impulse signal with an infinite frequency band, and also neglects interferences between the acoustic waves reflected at different levels. Actually, the thermocline seismic response measured at a receiver is  $R(t) = s(t) * \eta(t)$  where the seismic source  $s(t)$  is characterized by a limited frequency bandwidth. As already highlighted in many previous works on complex reflectors, and in particular by [Hobbs *et al.*, 2009] and [Piété *et al.*, 2013] on thermohaline interfaces, the seismic response depends

sensitively on the structure of the reflectors, on the frequency content generated by the seismic source device, and on the depth of the target due to geometrical spreading of the seismic wave as discussed below.

This study has been recently developed by Ker *et al.* [2015] on the ASPEX and IFOSISMO thermoclines, analyzed in the framework of the Wavelet Response (WR) method introduced by Le Gonidec *et al.* [2002], an effective tool to assess the frequency-dependent reflection coefficient of complex reflectors [see Ker *et al.*, 2012 and the references herein]. The WR method, based on the wavelet transform properties, is a direct multiscale sounding of the medium characterized by an acoustic impedance profile fully defined from the hydrographic parameters T, S, and P. The source signals  $\psi_a(t) = \frac{1}{a}\psi(t/a)$  are dilated versions of an analyzing wavelet  $\psi(t)$ . For a Ricker analyzing wavelet  $\psi(t) = \frac{a^2}{\pi^2} e^{-t^2}$  comprising three extrema, a wavelet reference frequency (here a peak frequency) is given by  $F_p = 1/\pi a$ , where  $a$  is a dilation factor [Ker *et al.*, 2012]. For sake of clarity in the rest of the paper, the term “frequency” stands for the peak frequency when dealing with the WR analysis.

The wavelet response  $R[\psi, \gamma](t, a)$  is computed following the Goupillaud approach [Goupillaud, 1961] in order to successively propagate each wavelet source signal of the wavelet family through the medium and record the successive back-reflected signals. Note that according to section 3.1 and the previous work by Ker *et al.* [2015], this multiscale seismic response of an acoustic impedance profile  $\gamma$  expressed in the time domain can be approximated by the wavelet transform of the temperature gradient  $\frac{\partial T}{\partial z}$ , i.e.:

$$R[\psi, \gamma](t, a) \iff a W \left[ \psi, \frac{\partial T}{\partial z} \right] (z, a) = \psi \left( \frac{t}{a} \right) * \frac{\partial T}{\partial z}, \quad (1)$$

where  $*$  stands for the convolution operator. The amplitude of  $R$  as a function of the wavelet dilation  $a$  is the so-called ridge function [Mallat, 1998; Mallat and Hwang, 1992].

To illustrate this WR analysis, we can consider a simple thermocline model structure for which  $\frac{\partial T}{\partial z}$  is prescribed as a “window” discontinuity of thickness  $\Delta z$  [see Le Gonidec *et al.*, 2002 for a full description]. For seismic wavelengths  $\lambda \gg \Delta z$ , the WR shows a cone-like structure pointing toward the center of the discontinuity which is equivalent to an ideal impulse, i.e.,  $\frac{\partial T}{\partial z} \sim \delta(z)$ : according to equation (1), the slope of the ridge function is  $\alpha = +1$ . When  $\lambda \ll \Delta z$ , this conical structure splits into two conical substructures pointing toward the rising and falling edges of the window function, respectively, and  $\alpha = 0$ . In the intermediate range  $\lambda \sim \Delta z$ , the WR is controlled by wave interferences with the edges of the window discontinuity: the ridge function, introduced as a multiscale seismic attributes in [Ker *et al.*, 2011], can be used to identify the characteristic size  $\Delta z$  of the thermocline-related reflector [Ker *et al.*, 2012].

### 3.3. Multiscale Seismic Amplitude of Thermoclines

As a first application, we perform the synthetic multifrequency seismic analysis of a hydrographic profile finely described by high resolution in situ measurements of T, S, and P: actually, the depth sampling of the profile, which belongs to the HR data set, is as good as 30 cm, allowing high-frequency wave propagation in the numerical approach. Indeed, the depth sampling  $\delta z$  of in situ hydrographic measurements defines the maximum frequency  $f_{\max} \simeq 1500/2\delta z$  for the wave propagation: it has to be noted that we performed the seismic modeling by using a correct sampling of the grid size ( $< \delta z$ ) to prevent from spatial aliasing of the wavefield. It is thus reasonable to perform the wavelet response analysis of the HR hydrographic profile with wavelet frequencies up to 1000 Hz: in comparison,  $\delta z = 1$  m of the LR data set limits the frequency to 300 Hz, and  $\delta z = 10$  m of usual ARGO data would limit the analysis to frequencies as low as 30 Hz. On the other hand, the low-frequency boundary is fixed to 50 Hz as previously used in Ker *et al.* [2015]. The WR analysis of HR hydrographic profiles is thus performed with Ricker wavelets in the broad range of frequencies, i.e., 50–1000 Hz.

The WR represents the back-reflected signal, in the two-way travel-time of propagation between the source transmitter and the reflector, as a function of the logarithm of the frequency of the seismic wavelets: as discussed above, it is controlled by the hydrographic parameters T, S, and P, which are taken into account in the numerical approach. For the particular HR profile analyzed here (see its temperature gradient in Figure 6a), a main cone-like structure is clearly highlighted in the WR displayed in Figure 6b. At low frequencies, it points toward the main detectable feature of the thermocline-related seismic reflector located at water depth 32 m. At higher frequencies, the main structure splits into conical substructures due to the complex

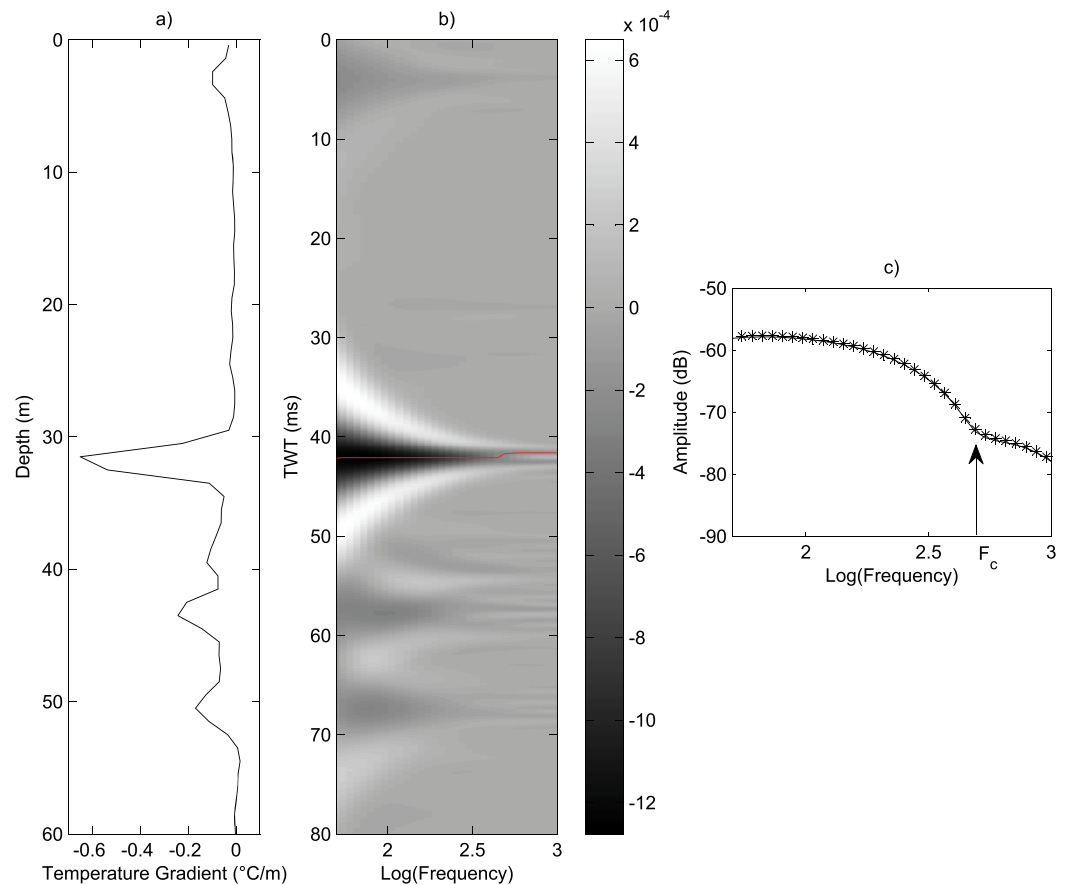


**Figure 6.** Multifrequency analysis of a temperature profile of the HR data set: (a) vertical temperature gradient, (b) associated wavelet response in the seismic frequency range 50–1000 Hz, the main cone-like structure is associated to the main temperature gradient centered at the depth 32 m, the weak reflectivity features observed in the WR result from interactions between the seismic wavelets and the fine-scale structure of the complex temperature gradient. (c) Multiscale Seismic Amplitude along the dominant ridge function (red line displayed in Figure 6b): the symbols represent the ridge function defined from the wavelet response analysis of the temperature parameter alone (approximation expressed by equation (1)). The arrow locates the corner frequency  $F_c$ .

morphology of the thermocline reflector. The frequency variations of the maximum amplitude of this multifrequency structure (Figure 6b, red line) are the so-called ridge function: we call this dominant ridge function the Multiscale Seismic Amplitude (MSA) of the hydrographic profile (Figure 6c, solid line). Since the MSA is not a straight line, it suggests a hydrographic profile characterized by a multiscale structure assessed in the frequency range 50–1000 Hz. The MSA is nearly flat and constant to  $-58$  dB for seismic frequencies lower than 100 Hz where the thermocline reflector is seen as a simple step-like discontinuity. Up to the corner frequency  $F_c=450$  Hz, the MSA continuously decreases down to  $-75$  dB, where the fine structure of the thermocline reflector starts to impact the acoustic wave propagation, i.e., the acoustic waves are sensitive to the weak individual subinterfaces composing the thermocline rather than to the large “bulk” temperature discontinuity. This numerical result of the MSA (Figure 6c, solid line), based on the knowledge of the three hydrographic parameters  $T$ ,  $S$ , and  $P$ , can be compared to the analytic result from equation (1) based on the temperature measurement only (Figure 6c, symbols). Both results are in very good accordance, strengthening the fact that the seismic analysis is mainly controlled by the temperature profile, i.e., by the thermocline structure.

Actually, the frequency dependence of the MSA of seasonal thermocline reflectors has already been discussed in Ker *et al.* [2015] on the basis of the ASPEX and IFOSISMO thermocline structures: the authors showed that modeling the dominant temperature step of the ASPEX temperature profile by a Gauss Error Function led to a MSA shape which agreed well with the ASPEX MSA in the frequency range 50–1000 Hz. But in the present study, based on a larger set of profiles, we highlight that this Gauss Error Function model does not always provide a satisfactory acoustic description of the thermocline over the entire frequency

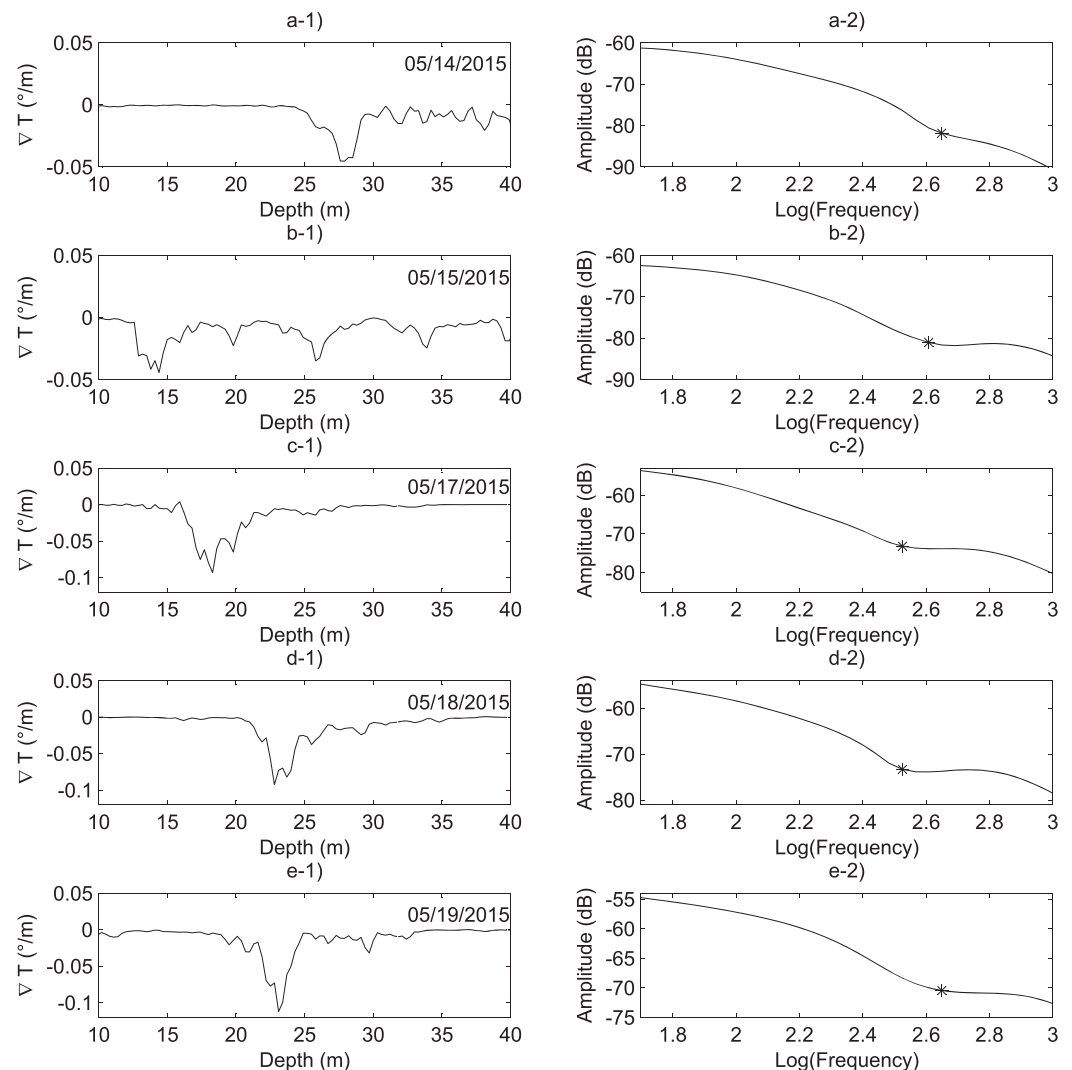


**Figure 7.** (left) Temperature gradient ( $^{\circ}/m$ ) as a function of the water depth (resolution 30 cm). The date is the date of the measurement performed at sea in 2015. (right) Seismic reflectivity associated to the main temperature gradient contrast as a function of the seismic frequency (range 50–1000 Hz), i.e., the MSA curves which are characterized by a corner frequency  $F_c$  (symbol).

range: indeed, since the model does not describe the fine-scale structures of a complex thermocline, it cannot highlight the corner frequency  $F_c$  over which the MSA shape is very sensitively dependent to the details of the temperature gradient structure. This observation, based on the MSA curve of Figure 6c, is supported by a set of five other gradient profiles also belonging to the HR data set (Figure 7a): though below the corner frequency  $F_c$  the MSA curves (Figure 7b) have similar, regular shapes,  $F_c$  values differ, and the irregular behavior at frequencies higher than  $F_c$  seems to preclude a deterministic description. We thus turn in the following section to a description of the statistics of MSA curves, with the aim to provide a description of the typical range of variability of the seismic reflectivity of the shallow thermohaline structure of the ocean at a midlatitude location.

#### 4. Multiscale Seismic Amplitudes of Seasonal Thermoclines Reflectivity

##### 4.1. Statistical Characteristics of Seismic Amplitudes Estimated From the High-Resolution Profiles

The wavelet-based analysis described above allows both characterizing the strength, from the MSA, and locating the main reflector of a thermocline profile, i.e., the dominant temperature gradient which controls the seismic response. In order to assess quantitatively the effect of “random” perturbations, such as small-scale structures, internal gravity waves, meteorological events, or interannual variability of its characteristics,

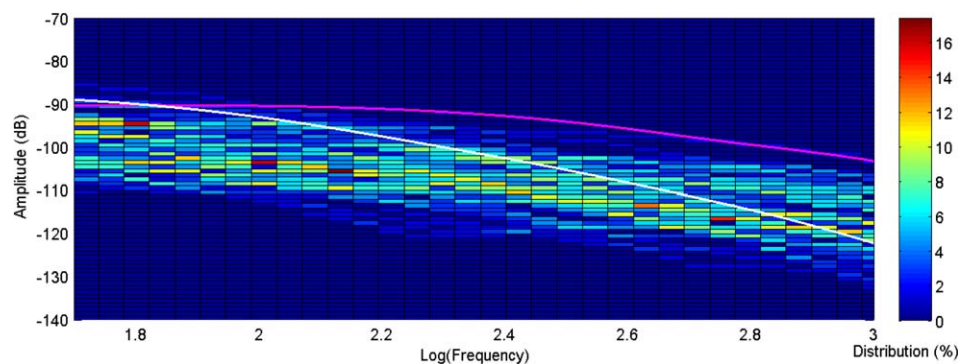


**Figure 8.** Distribution of MSA values determined from the HR data set (69 thermocline profiles): the MSA curves associated to the ASPEX and IFOSISMO temperature profiles are indicated in magenta and white, respectively.

on the seismic detectability of the seasonal thermocline in an ocean region, we now turn to a statistical analysis of the wavelet response of 69 featured thermoclines belonging to the HR data set. Note that the 37 other profiles do not highlight any clear temperature contrasts and thus, could not be processed.

Most of the sources of variability listed above are naturally present in the hydrographic measurements and are transparently carried over to the MSA by the WR processing. An effect that must however be taken into account separately is the variability in the depth location of the thermocline which, as highlighted in Figure 3 for instance, can range roughly between 10 and 60 m of water depth in the data set. Since acoustic propagation in the water induces an attenuation of the seismic wave amplitude by spherical spreading, the acoustic power received at the detector for deep reflectors tends to be smaller than that for shallow ones of comparable strength. Neglecting this effect does not alter the shape of the MSA curve and allows focusing on the MSA morphology in term of multiscale seismic attributes: however, this effect has to be taken into account, by applying to the “raw” WR a  $20\log(2z)$  dB correction, in order to compute and quantitatively compare actual MSA curves as performed in the following.

The distribution (in percentage of the number of profiles actually featuring thermoclines) of the depth-corrected seismic reflection amplitude as a function of the seismic frequency (50–1000 Hz) shows a general decreasing tendency from  $-100$  to  $-120$  dB with a dispersion limited to about 20 dB (Figure 8). For example, at the high resolution seismic frequency of 500 Hz, roughly 10% of the thermocline reflectors are associated to a MSA comprised between  $-110$  and  $-109$  dB.

Even if a coherent behavior of the MSA curves can be highlighted, the statistics based on the HR data set alone do not seem sufficient to describe a clear MSA pattern representative of seasonal thermoclines. As already mentioned before, this high-resolution study has however the interest to be directly applicable to the ASPEX and IFOSISMO CTD profiles, i.e., their MSA curves (Figure 8, magenta and white curves, respectively) can be quantitatively compared to the ones of the whole HR data set. A first remark is that the MSAs produced from the ASPEX and IFOSISMO profile—collected using a lowered CTD profiler in 2012 in opposition to a free drifting float profiler and in 2015—have a behavior that is generally within the envelope of the HR data set, but they tend to feature particularly strong reflectivity values. As a second remark, since these two previous cruises aimed at the seismic study of the seasonal thermocline, particular care has been taken to purposefully perform them at moments when temperature contrast could be expected to be stronger than average (mid-June for ASPEX, end of summer for IFOSISMO): the explanation for the success of the ASPEX cruise probably lies in the exceptionally strong temperature gradient at the thermocline which makes the seismic reflectivity exceptionally high at all frequencies, as shown by the MSA curve plotted in Figure 8 (magenta curve). In particular, the reflectivity remains high even at the 470 Hz seismic frequency of the Sparker used for the ASPEX experiment: as discussed in Ker *et al.* [2015], this is linked to the extreme sharpness of the temperature gradient at the OSBL base during this cruise, which immediately followed a strong storm ( $H_s$  values in excess of 4 m being recorded at a nearby wave buoy less than 2 days before).

This result, which highlights the uniqueness of the thermocline detected in the ASPEX case with a 470 Hz Sparker source, needs to be strengthened by the consideration of the larger LR data set of hydrographic profiles.

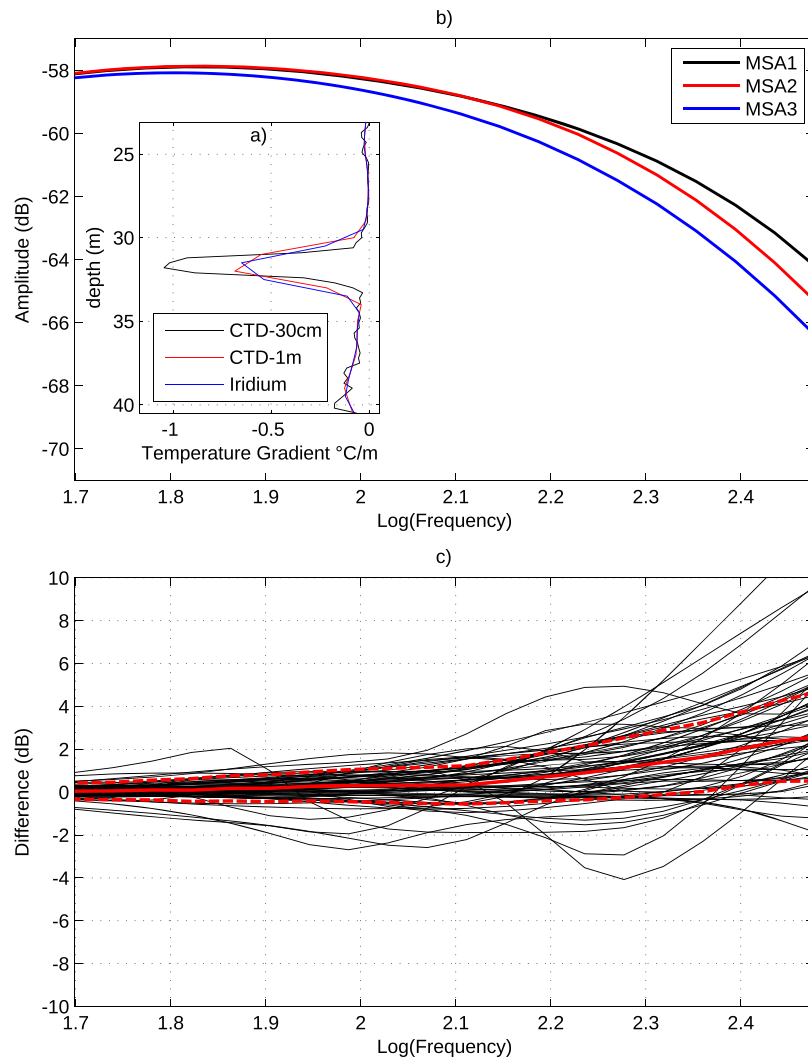


**Figure 9.** (a) One HR thermocline for three different configurations: (i) using the initial HR resolution of 30 cm (black), (ii) undersampling the data to 1 m with an anti-aliasing filter (red), and (iii) bin-averaging the data to 1 m according to the Iridium protocol (blue). (b) MSA curves associated to the three different configurations, i.e., (i) MSA1 (black), (ii) MSA2 (red), and (iii) MSA3 (blue). (c) Differences between MSA1 and MSA3 for the 69 thermoclines of the HR data set: the red curve indicates the median values.

#### 4.2. Impact of the Thermocline Resolution on the Seismic Amplitude

The previous MSA analysis dealt with the HR data set, acquired with a depth sampling interval of 30 cm but limited to 106 profiles, of which only 69 featured thermoclines. For a more representative analysis, the LR data set retrieved from the ARGO data centers and composed of 892 profiles featuring 616 thermocline observations (the other profiles do not highlight any clear temperature contrasts and thus, could not be processed), is a natural extension of this study: but these hydrographic measurements have undergone data reduction to 1 m depth sampling interval prior to Iridium transmission to ground. As a consequence, the extension of the study is not straightforward and requires a particular care. Indeed, we have shown that the seismic response is sensitive to the fine-scale structures of the temperature profile, and we have to check to what extent the results of the synthetic multiscale analysis depend on the data set resolution.

To do so, i.e., in order to quantify the impact of the data set resolution on the MSA analysis prior extending it from the HR data set to the LR data set, we compute the MSA of each HR thermocline through three different procedures: (i) by using the initial HR resolution of 30 cm, (ii) by undersampling the data to 1 m with an anti-aliasing filter, and (iii) by applying the 1 dbar bin-averaging data reduction procedure implemented in the floats. As mentioned in the introduction of the MSA in section 3.3, the depth sampling interval sets the frequency range of the multiscale analysis, which is reduced to (50–300 Hz) for the LR data set. We

illustrate the impact of the procedure on the MSA with the thermocline profile already discussed in section 3.2 (see the thermocline's temperature gradient in Figure 6a): Figure 9a displays this profile when processed according to the three different procedures, and Figure 9b displays the associated MSAs (MSA1, MSA2, and MSA3, respectively).

The MSA1 (Figure 9b, black curve) of the HR thermocline is the ridge function displayed in Figure 6c. The MSA2 is slightly modified, in particular for frequencies higher than 150 Hz (Figure 9b, red curve): the anti-aliased undersampling procedure partially filters the thermocline fine-scale features and thus decreases the high-frequency amplitudes of the MSA. The impact of the bin-averaging protocol is much more pronounced: the MSA3 is affected at all frequencies, up to 2 dB at 300 Hz (Figure 9b, blue curve). This clearly highlights the loss of information incurred when the thermocline profile is decimated using simple bin-averaging: the seismic amplitude predicted by the wavelet response method performed on the LR data set underestimates the thermocline reflector strength and we suspect that other types of spectral analyses of ARGO profiles might be affected in similar ways.

As a direct recommendation, we suggest that the bin-averaging procedure, which is widely used in most oceanographic studies, should be replaced by a properly anti-aliased undersampling procedure. This observation can be generalized to the whole HR data set and we quantify the discrepancy by determining the difference between MSA1, based on the HR data set and MSA3 based on the associated LR version (Figure 9c): undersampling the data from 0.3 to 1 m leads to a median discrepancy (Figure 9c, red curve) close to zero for frequencies lower than 150 Hz, where the impact of the data resolution can thus be neglected, increasing with the frequency up to 2.5 dB at 300 Hz, i.e., a low resolution of the thermocline profile leads one to underestimate the seismic reflection amplitude. As a first approximation, the median curve can be used as a bias corrector when dealing with the LR data set, in particular as we study the thermocline detectability issue in section 6.

### 4.3. Seasonal Variations of Thermocline Seismic Amplitudes

Based on the previous analysis developed from the high-resolution but limited data set, we are now in position to take benefit of the larger LR data set of ARGO profiles. As a preliminary approach to assess the seasonal variations of thermocline seismic amplitudes, we consider in this section the succession of 171 thermocline profiles acquired at the South site in 2012 (Figure 2d). The seismic response of the dominant feature of each thermocline, i.e., the MSA, is determined in the limited frequency range 50–300 Hz, as discussed in the previous sections.

In a first step, the MSAs are computed without taking into account the spherical spreading attenuation in order to only characterize the temperature gradient according to equation (1) (Figure 10a): this highlights a general decrease by 34 dB (–53 to –87 dB) of the thermocline reflector strength over the seismic source frequency range 50–300 Hz. A first remark is that the seasonal cycle in temperature, which is clearly evident in the temperature profiles (Figure 2b), does not immediately translates into a seasonal dependence of the seismic reflection amplitude, at least at low frequencies: this is probably in part explained by the almost linear relationship between thermocline thickness and temperature contrast evidenced in (Figure 3b). This linear relationship indicates a tendency for the temperature gradient (hence low-frequency seismic response) to remain almost constant during the fall-winter destratification phase. This seems to indicate that, at this scale of observation, there is no obvious correlation between the seasonal conditions and the reflectivity of the dominant seismic feature of a thermocline.

In a second step, however, the MSAs are corrected to take into account the spherical spreading attenuation of the seismic wave which depends on the depth location of the thermocline reflector: in that case, the observed range of seismic amplitudes expands to ~40 dB (–88 to –130 dB), which shows the sensitivity of the MSA to the spherical spreading attenuation. In addition, a stronger seasonal dependency is now observed (compare the much reduced MSA values after day 280 in Figure 10b), which is related to the thermocline depth seasonal cycle.

As a conclusion to this section, the analysis of MSA curves informs about two scales of observations. The first one is the fine-scale structure of the thermocline, assessed from high seismic frequencies and controlled by complex dynamic processes which induce the MSA variability observed between successive measurements: to go further into this analysis, high-resolution measurements would be required both in

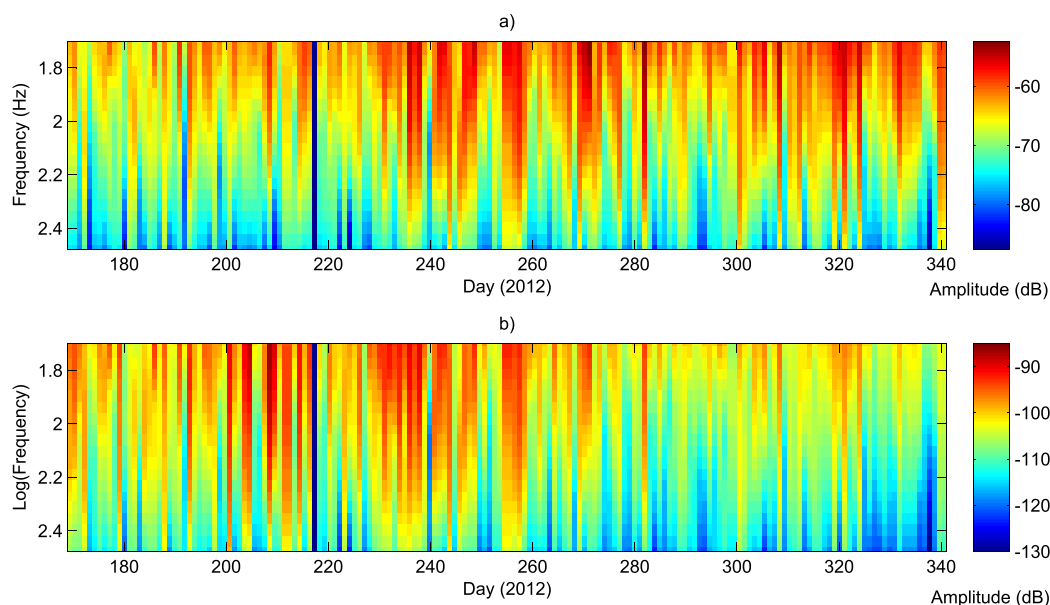


**Figure 10.** MSA values of the 171 thermoclines of the LR data set acquired in 2012 at the South site: (a) without and (b) taking the spherical spreading attenuation of the seismic wave into account.

space (along the water column) and time (recurrence of the measurements). The second one is the large-scale structure of the thermocline related to seasonal processes which control the depth of the thermocline reflector, i.e., which induce a global amplitude shift of the MSA.

#### 4.4. Generalization of the Statistical Study of Seismic Amplitudes

We now extend the analysis to the whole LR data set of thermocline profiles collected on the Armorican Shelf, comprising 616 profiles measured with the bin-averaged depth sampling of 1 m. For each profile, both the seismic reflection amplitude of the dominant thermocline feature and its depth location are automatically extracted using the wavelet-based method: we thus get 616 MSA curves in the frequency range 50–300 Hz. Note that the MSA values take into account the spherical spreading attenuation of the wave propagation and are corrected from the resolution bias (Figure 9b, red curve) induced by the pretransmission bin-averaging.

Figure 11a displays a scatter plot of the MSA location (defined at 100 Hz from the WR analysis) versus the OSBL/thermocline boundary  $z_{min}$  computed from the temperature profiles as described in section 2.5. The agreement between the two estimates is striking, if one takes into account the fact that the temperature-threshold method is designed to pinpoint the depth of the upper limit of the thermocline, whereas the MSA-based methods detects the depth of its maximum temperature gradient, i.e., an object which is deeper by construction.

The probability distribution of MSA values as a function of the seismic source frequency in the range 50–300 Hz is presented for the LR data set in Figure 12a, and recalled for the HR data set in Figure 12b. At all frequencies, the MSA values are distributed within a 20 dB range centered on a ridge going from  $-100$  dB at 50 Hz to  $-113$  dB at 300 Hz. The location of the maximum probability ridge depends linearly on the logarithm of frequency to a good approximation: MSA values on the ridge are highly probable, with probability values commonly reaching 10% of the profiles per 1 dB bin in that area. It is interesting to note the good agreement with the previous analysis limited to the 69 thermoclines of the HR data set, for which the statistical basis was not sufficient to reliably locate the distribution peak (Figure 12b). This result shows the robustness of our statistical approach which consists in combining different thermocline data sets acquired at different sites and years. The multifrequency seismic amplitude of the thermocline reflector defined from the MSA distribution is thus a representative proxy which can be used to assess the seismic detectability of midlatitude seasonal thermoclines. At each frequency  $f$  in the range 50–300 Hz, the distribution of the seismic reflection amplitude (in dB) of the seasonal thermocline on the Armorican Shelf is well approximated by a normal distribution with an average MSA curve defined by:

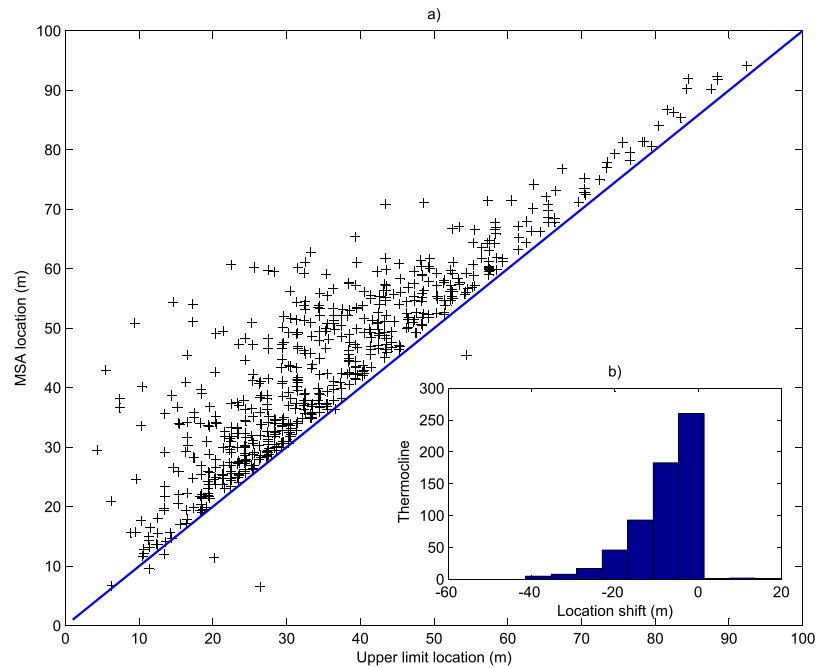


**Figure 11.** Thermocline parameters estimated for the thermoclines of the whole LR data set: (a) crossplot between the thermocline upper limit defined from the temperature profiles and the MSA depth location based on the wavelet-based method and (b) histogram of the differences between these two parameters.

$$\langle MSA \rangle = -14.8 \log(f) - 73.4 \tag{2}$$

and a standard deviation about 5.5 dB.

## 5. Seismic Experiment Capability (SEC) to Detect Thermoclines

### 5.1. Basic Principles

Seismic detectability of shallow oceanographic structures has been investigated in Piété *et al.* [2013] based on the sonar equation [Urlick, 1983; Lurton, 2002] which provides a framework to estimate the echo level measured at a seismic receiver associated to a seismic reflector which back-reflects an acoustic wave emitted by a seismic source:

$$S_r = G_r(\theta) + S_0 + G_s(\theta) - 20 \log(d(\theta)) + R(\theta) \tag{3}$$

where  $S_r$  is the echo sound level (in dB re  $\mu\text{Pa}$ ) measured at the receiver associated to the gain factor  $G_r$ . Note that the receiver, characterized by a directivity index (in dB) and a sensitivity (in dB re  $1\text{V}/1\mu\text{Pa}$ ) which controls the output voltage, can detect underwater signals in a restricted frequency range in accordance with the frequency content of the seismic source. The parameter  $S_0$  is the strength (in dB re  $1\mu\text{Pa}$  @ 1 m) of the seismic source characterized by a gain factor  $G_s$ . The term  $-20 \log(d(\theta))$  corresponds to the spherical attenuation of the acoustic wave, i.e., the geometrical spreading of the sound energy: the distance  $d$  stands for the sum of (i) the distance between the seismic transmitter to the target, which reflects the acoustic wave incident with an angle  $\theta$ , and (ii) the distance from the target to the seismic receiver. The last term  $R$  stands for the strength, or reflectivity (in dB), of the target.

As a first approach, it is commonly observed that the reflectivity  $R$  is higher at low frequencies than at high frequencies: in the present study, we quantify the frequency dependency of  $R$  for shallow seasonal thermocline targets using the multiscale seismic amplitude, i.e., the last two terms of equation (3) correspond to the MSA discussed in details in the previous sections. The angular dependency of the reflectivity is out of the scope of the present paper which deals with the monostatic case where  $\theta=0^\circ$  (and stack sections) and the seismic transmitter and receiver are at the same location. We group the other terms of the sonar equation into a parameter noted  $S$  which includes  $S_0$ ,  $G_r$  and  $G_s$  but also additional processing gains such as

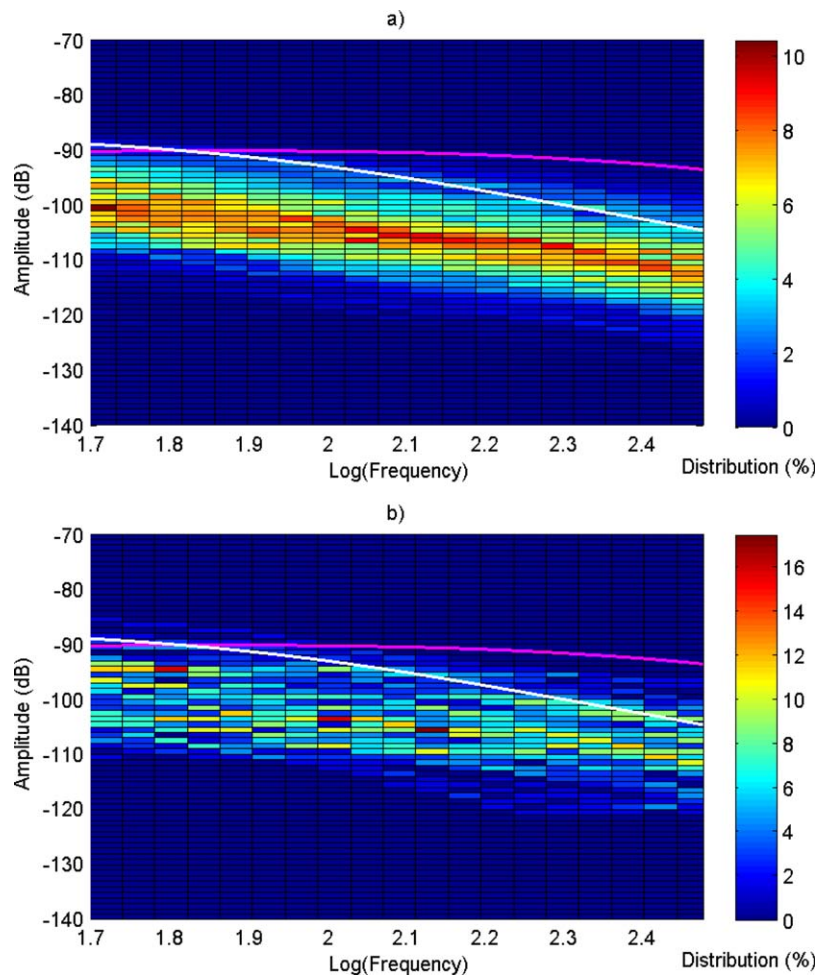


**Figure 12.** Distribution of the MSA values defined in the frequency range 50–300 Hz from (a) LR and (b) HR data sets. The curves associated to ASPEx and IFOSISMO are represented by the magenta and white curves, respectively.

the directional gain, based on the directivity index and beamforming processing, filtering procedures (band-pass and common midpoint sorting), summation procedure of normal moveout correction, stacking operation, and migration [Yilmaz, 1987; Piété et al., 2013].

As a result, one is led to define as “detectable” a reflector whose MSA satisfies  $S + MSA \geq \mathcal{T} + \mathcal{N}$ , where  $\mathcal{T}$  is the detection threshold and  $\mathcal{N}$  the detected noise level of the seismic experiment. The detection threshold can be expressed by  $\mathcal{T} = 10 \log(\text{signal power}/\text{noise power})$ : considering a ratio of 4, i.e., the mean signal amplitude is twice the mean noise amplitude,  $\mathcal{T} = 6$  dB is a common value widely used in acoustic detection.

A final logical step is to gather the terms that are independent of the reflector in a single quantity which defines the seismic experiment capability (SEC) to detect thermoclines: the SEC parameter is thus defined as

$$SEC = S - \mathcal{N} - \mathcal{T} \tag{4}$$

Using this definition, a reflector of strength  $MSA$  can be seismically detected if the SEC parameter characterizing the involved seismic experiment satisfies the condition

$$SEC + MSA \geq 0. \tag{5}$$

### 5.2. Quantitative Assessment of the SEC Parameter

As defined above, the SEC parameter of a seismic experiment takes into account the overall acquisition conditions, including (i) the seismic source strength and frequency bandwidth, (ii) the fold parameter of an

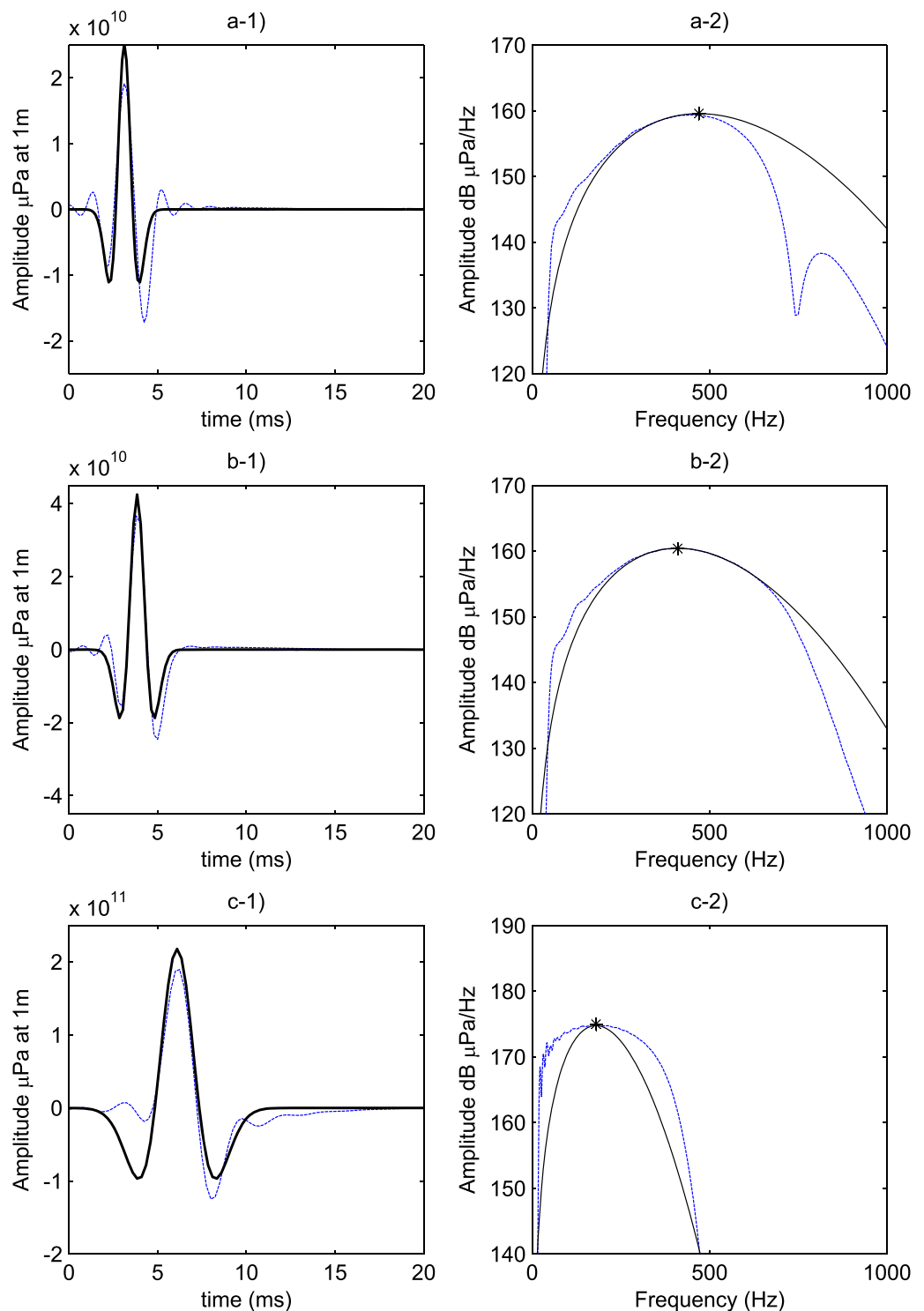


**Figure 13.** (left) Seismic source signatures in the time domain and (right) associated amplitude spectra in the Fourier domain for two different VHR Sparker sources used in (a) ASPEX and (b) IFOSISMO, and for a HR airgun source (c) modeled with the software Gundalf<sup>TM</sup>. A seismic source is characterized by both a source strength  $S_0$  and a peak frequency  $F_p$  which are defined by the peak-to-peak amplitude and by the frequency of maximum amplitude spectrum, respectively. The black curves correspond to the Ricker approximation.

MCS setup, which corresponds to the number of shot-receiver pairs that illuminate a given point of the medium, and (iii) the noise level. This section provides quantitative assessment of these three contributions in order to estimate actual SEC parameters of seismic experiments performed at sea to detect seasonal thermoclines.

**Table 2.** Parameters Defined for Three Seismic Experiments: Two Very High-Resolution Experiments (ASPEX and IFOSISMO) and One Synthetic High-Resolution Experiment (Synthetic), Involving Different Seismic Source Signatures Approximated to Ricker Wavelets and Called *Ricker1*, *Ricker2* and *Ricker3*, Respectively (see Figure 13).

	Experiment	Source Signature	$S_0$ (dB)	$F_p$ (Hz)	Fold Gain (dB)	Noise (dB)	SEC (dB)
VHR	ASPEX	Ricker1	210	470	16	120	100
	IFOSISMO	Ricker2	213	410	16	126	97
HR	Synthetic	Ricker3	230	180	20	121	123

### 5.2.1. Strength and Frequency Bandwidth of the Seismic Source

We remind that the present work deals with a high and a low-resolution data sets (see Table 1), which can be analyzed in the frequency range 300–1000 Hz and 50–300 Hz, respectively: in the framework of the WR analysis, these frequencies correspond to peak frequencies of Ricker wavelets used as seismic sources. When dealing with seismic imaging of shallow thermohaline structures, two kinds of actual seismic systems can be deployed at sea, i.e., very high-resolution (VHR) and high-resolution (HR) seismic systems: in the following, these systems are associated to the above frequency ranges, respectively.

The aim of the present section is quantifying, for these two kinds of seismic systems, the acoustic properties of actual seismic sources, including not only the frequency content, which can be assessed from Ricker waveforms, but more particularly the strength  $S_0$ . To do so, we use three different seismic source signatures. The two first signatures belong to the VHR domain and were designed for imaging shallow thermoclines during the ASPEX and IFOSISMO experiments (blue curves in Figures 13a1 and 13b1, respectively): they correspond to different configurations of a Sparker source, i.e., different source powers and electrode designs, aiming at obtaining different source strengths and peak frequencies [Thomas et al., 2013]. The third signature belongs to the HR domain and stands for the signature of a small airgun which has already been used in seismic oceanography, during GO-HR and Carambar experiments for instance [Géli et al., 2009; Piété et al., 2013], for its good trade-off between source strength and high-frequency content (Figure 13c1, blue curve): as no far field measurement of the airgun source was available from the Carambar data set, the signature has been synthesized by the modeling software Gundalf<sup>TM</sup> for a small airgun source MiniGI 24/24 ci towed with an immersion depth of 1.5 m, providing an accurate source signature within the experimental errors of in situ measurements [Ziolkowski et al., 1982; Laws et al., 1990].

The source strength  $S_0$  of the seismic source signature is defined in the time domain as the peak-to-peak amplitude, i.e., the difference between the maximum and minimum amplitudes expressed in dB re  $1\mu\text{Pa}$  @ 1 m (Figures 13a1, 13b1, and 13c1). Based on this definition,  $S_0$  does not result from a single frequency but instead, it includes the frequency bandwidth of the source signature defined in the Fourier domain (Figures 13a2, 13b2, and 13c2, blue curves): nevertheless, according to the WR analysis where the wavelet source signal is defined by a peak frequency, we associate the source strength with the central frequency of the bandwidth, i.e., the peak frequency  $F_p$  which is indicated by a star in the frequency spectrum (Figure 13). As a result, the source strength  $S_0$  and the peak frequency  $F_p$  of the three seismic source signatures belonging to the VHR/VHR/HR domains are 210/213/230 dB and 470/410/180 Hz, respectively (see Table 2).

In the WR multiscale method developed in the present work, the analyzing wavelet was defined as a Ricker signal, the reason being that it is commonly used in seismic exploration to approximate a seismic source signal [Wang, 2015]. We define the Ricker wavelet which approximates a source signature by both  $S_0$  and  $F_p$  (Figure 13, black curves): as a first approach, the approximation is satisfactory and in the following, the source signatures are called *Ricker1*, *Ricker2*, and *Ricker3*, respectively. The discrepancy is not of first importance since the paper focuses on the MSA, which is related to the main amplitude of the WR analysis. Thus, the condition equation (5) makes sense when dealing with the peak frequency of a seismic source signature approximated to a Ricker wavelet.

### 5.2.2. Fold Parameter of the Multichannel Setup

The weakness of thermocline-related reflector requires improving the signal-to-noise ratio in the data acquisition. In seismic imaging, this is commonly achieved by the use of a multichannel acquisition setup characterized by the fold parameter that measures the redundancy of common midpoint seismic data, equal to the number of shot-receiver pairs that illuminate the same point of the medium. In theory, a fold of order  $m$  enables increasing the signal-to-noise ratio by a factor  $20\log\sqrt{m}$  ([Yilmaz, 1987]). For instance, a gain of 20 dB can be expected for multichannel seismic experiments performed with a fold of 100. In practice, this

gain could be lower, depending on the data and related processing sequence but as a first approximation, we consider that the fold parameter mainly contributes to the global processing gain of the system (estimated by *Thomas et al.* [2013] about 16 dB for ASPEX and IFOSISMO), and is called the *fold gain* in the following. The approximation of the processing gain by the fold parameter has the interest to allow studying the impact of the fold on the thermocline detectability as detailed in section 6.

### 5.2.3. Noise

The ambient noise level  $\mathcal{N}$  is another parameter which controls the seismic detectability of a thermocline (equation (4)). The detected noise level is the result of different sources of noise [Wenz, 1962], classified here in three main classes for the frequency range of the present study, i.e., 50–1000 Hz. The first class deals with water mass motions, i.e., with hydrodynamic sources: atmospheric turbulences, such as winds, induce surface waves, subsurface pressure fluctuations, etc. The second class is the ambient noise induced by marine life, volcanic/tectonic activity, bubbles, breaking waves, but also shipping activity, off-shore drilling rigs, etc. The third class is the self-noise generated by the receiving platform submitted to water current flow around it and induced mechanical vibrations. Quantitative assessments of the noise levels show a frequency dependency [Wenz, 1962], a wind-dependent and a nonwind-dependent sources [Perrone, 1969], and a slight increase of about 0.2 dB/yr [Chapman and Price, 2011], in particular due to a continuous development of the shipping activity. As a consequence, these noise levels, which fluctuate with both time, space, and frequency, are not straightforward to assess but cannot be neglected for passive acoustic measurements: in the present case of active seismic experiments, the dominant source of noise comes from the research vessel and the attached seismic device, i.e., it mostly consists in local self-noise. Indeed, surface waves can induce turbulent pressure fluctuations or actual mechanical shocks along the seismic system, inducing a stability loss which depends on the sea state and can generate a dominant noise contribution.

In order to assess the recorded noise level  $\mathcal{N}$ , we take benefits of several quantitative analyses performed by IFREMER during the last 10 years, performed in the framework of quality control of the seismic data. In these analyses, which did not estimate the frequency dependency of  $\mathcal{N}$ , noise strengths were defined in the time domain, similarly to  $S_0$ , in the frequency bands of different HR and VHR seismic devices. As a result, the mean noise level is quantified in the frequency range 50–1000 Hz and takes into account the three classes of noise introduced above: measured between 106 and 114 dB when the seismic experiments are performed with perfect sea conditions (World Meteorological Organization sea state code = 0), the mean noise level increases up to 128 dB when measured with moderate sea conditions (World Meteorological Organization sea state code = 4). Note that for rough sea conditions (sea state >5), we consider that no seismic experiment can be performed. In order to ensure  $\mathcal{N}$  to be higher than the noise level from ship or ambient noise [Biescas et al., 2016; Wenz, 1962], the present work deals with the noise level range 114–128 dB: characteristic of actual multichannel seismic experiments, it is used as a first approximation to quantify the noise level. This range is consistent with the ambient noise levels evaluated from the ASPEX and IFOSISMO experiments (Table 2), that is to say 120 dB and 126 dB, respectively [Thomas et al., 2013]. For the synthetic experiment using an airgun seismic source, we arbitrary fix the noise level to 121 dB, which stands for the intermediate level of ambient noise that could be encountered during seismic experiments.

We remember here that  $\mathcal{N}$ , as well as  $S_0$  and thus SEC, is defined in the time domain and associated to the peak frequency  $F_p$  of the Ricker-like seismic source signature, in accordance to the MSA developed in the framework of the wavelet response: a frequency dependency analysis of the noise level, when required data are available, can be performed to specify the SEC value but is not necessary, as discussed in the following section, because the present analysis is already performed for a range of SEC values characteristic of actual multichannel seismic experiments.

### 5.3. SEC Parameter: Estimation and Discussion

The SEC parameter, which characterizes, by its own, the capacity of a seismic experiment to detect a thermocline-like reflector according to equation (5), includes the three parameters described above and summarized in Table 2: the SEC parameter increases with the source strength and the fold order, and decreases with the noise level, i.e., different configurations may give similar SEC values. Note that the source strength and the noise level can both be considered as frequency dependent to specify the SEC parameter of a given seismic experiment: this study would have asked for specific data that were not available for the present work, but the SEC parameter faces this limitation. We define the range of SEC values for both the VHR and HR domains using the seismic source signatures described above by considering the individual

parameters established for the experiments described in Table 2. The SEC parameters of the two VHR experiments ASPEX and IFOSISMO are estimated around 100 and 97 dB, respectively (Table 2), which means that the capacity of the former in detecting seasonal thermoclines is slightly better than that of the latter. For seismic experiments involving HR seismic sources, a representative SEC value can be estimated from the Synthetic experiment around 119 dB, which appears much more efficient in detecting thermoclines. Based on these characteristic parameters, we generalize the present study to other seismic experiments, i.e., to other SEC values, by considering two different SEC ranges as large as 20 dB: 90–110 dB for VHR experiments and 109–129 dB for HR experiments.

Actually, the efficiency of the HR experiments is not straightforward when imaging shallow reflectors such as the seasonal thermoclines of the Armorican shelf which can be as shallow as 10 m (Figure 3a). Compared to a high-frequency source, the limitation of a low-frequency source is not only due to a lower lateral (not studied here) and vertical resolutions, but also to the minimum depth required for the reflector location: as a first approximation, this depth is constrained by the signature duration of the emitted wave. Indeed, interferences between the direct and reflected waves impede the observation of thermocline-like reflectors: this effect, stronger for longer seismic signatures, can particularly be pronounced for seismic systems belonging to the HR domain (for instance, airgun sources induce long duration bubble oscillations) [Landrø, 1992]. In the present study, a seismic signature is approximated to a Ricker wavelet which duration can be estimated to  $3/F_p$ : this means that the HR signature Ricker3 ( $F_p = 180$  Hz) can potentially image thermoclines deeper than 25 m, which is the case for 90% of the thermoclines belonging to the analyzed data set. Note that for the VHR signature Ricker1 ( $F_p = 470$  Hz), the limit water depth is reduced to roughly 9 m. In the following, this  $F_p$ -dependent limitation is considered in addition to the condition given by equation (5) to assess the seismic detectability of shallow thermoclines.

## 6. Seismic Detectability of Midlatitude Seasonal Thermoclines

### 6.1. SEC and Peak Frequency Ranges for the Thermocline Data Set Analysis

The capability of a seismic experiment in detecting a thermocline is quantified by the SEC parameter discussed above. In this section, we now take benefit of the large data set of representative thermoclines for which we defined the MSA distribution: as expressed by equation (5), the condition for a seismic experiment to detect a thermocline is  $SEC + MSA \geq 0$ , where the multiscale parameter MSA is defined as a function of the frequency, i.e., the peak frequency  $F_p$  of the seismic source. We remember that the thermocline data set used in the present study to determine characteristic MSAs is composed of two subdata sets, analyzed in the following two sections, respectively. The former, composed of 69 thermoclines collected with a depth sampling of 30 cm, is analyzed in the VHR domain with peak frequencies in the range 300–1000 Hz and SEC values in the range 90–110 dB. The second one is larger, composed of 616 thermoclines collected with a larger depth sampling of 1 m, and is analyzed in the HR domain with peak frequencies in the range 50–300 Hz and SEC values in the range 109–129 dB.

For a seismic experiment defined by both a SEC parameter and a peak frequency  $F_p$ , we estimate from equation (5) the overall probability of detecting a seasonal thermocline, taking into account the limitation inherent to its depth location (see discussion in section 5.3): a detectability of 0% means that the seismic experiment has no chance to detect a thermocline, and in contrary, 100% means that the seismic experiment is perfectly designed to detect any kind of seasonal thermoclines.

### 6.2. Detectability of Seasonal Thermoclines With VHR Seismic Sources

For seismic sources belonging to the VHR domain, characteristic SEC values range between 90 and 110 dB, depending mainly on the source strength, the ambient noise level, and the fold gain. This means that with control of these parameters, one can study, as a function of the global SEC parameter, the thermocline detectability for a given seismic frequency  $F_p$ , and in particular for the VHR frequencies 470 and 410 Hz of the ASPEX and IFOSISMO experiments, respectively. This study is developed on a the data set limited to 69 thermocline profiles but collected with a high-resolution, i.e., MSAs are adapted to the VHR domain determined for peak frequencies in 300–1000 Hz (see Figure 8): this constitutes a first approach in quantifying the VHR detectability of seasonal thermoclines located on the Armorican Shelf. The results of the analysis put in evidence a similar behavior for the two frequencies (Figure 14a), with a detectability close to 0% for  $SEC \leq 96$  dB, around to 2% for

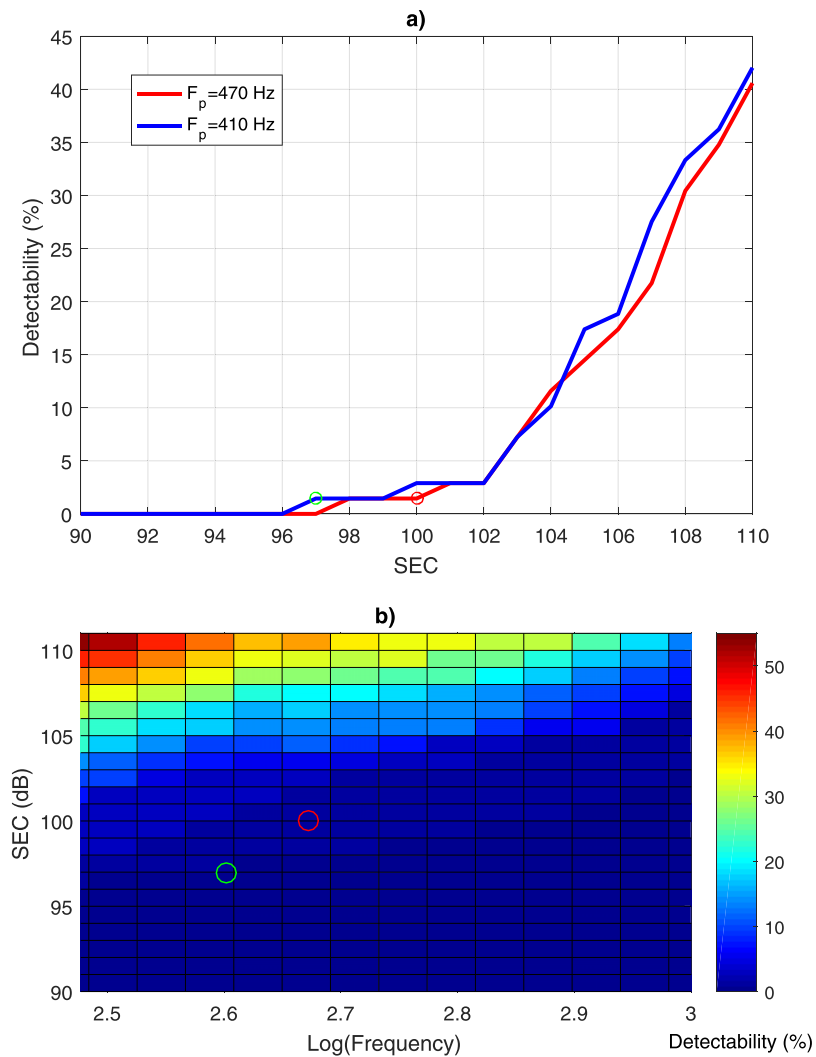


**Figure 14.** (a) Detectability determined from the MSA data set at two different peak frequencies  $F_p = 470$  Hz and  $F_p = 410$  Hz as a function of the SEC parameter (red and blue curves, respectively). The circles indicate the ASPEX (red) and IFOSISMO (green) Sparker experiments (see Table 2). (b) Detectability determined in the SEC range 90–110 dB and peak frequency range 300–1000 Hz associated to the VHR domain.

the SEC values associated to ASPEX and IFOSISMO (Figure 14a, red and blue circles, respectively), and a linear increase up to 40% between SEC = 102 dB and SEC = 110 dB.

Obviously, the success of ASPEX in detecting a seasonal thermocline in the VHR domain was a posteriori far from certain: this means that to promote the detection of shallow seasonal thermoclines, a VHR seismic experiment requires a SEC parameter much higher than 100 dB, that is to say a powerful seismic source, a high fold and a low ambient noise level. And indeed, the seismic capacity has to be at least twice that of ASPEX to improve the potential of VHR seismic experiments to a detectability close to 20%. We also observe that for SEC values lower than 104 dB, the detectability is not sensitive to the seismic frequency, while for higher values, the detectability is improved when using lower frequencies.

As a natural extension of this analysis, the approach is performed for the whole frequency range 300–1000 Hz of the VHR domain (Figure 14b). The duration of the source signature approximated to a Ricker wavelet is taken into account and thus limits the detectability in particular at low frequencies: in the VHR domain, the minimum depth required for a thermocline depth location is 15 m, which is the case for more than 93% of the thermocline belonging to the high-resolution CTD data set. This highlights that the frequency dependency of the detectability is controlled by the multiscale structures of the thermoclines captured by the

MSAs (Figure 8). Finally, the thermocline detectability remains below 55% in the VHR domain, with a maximum reached for a seismic frequency of 300 Hz and seismic experiment capacity of 110 dB. We remember that this result is based on 69 thermoclines only but makes sense since the associated MSAs are in agreement with the MSAs of the more comprehensive data set analyzed in the next section (see Figure 12).

### 6.3. Detectability of Seasonal Thermoclines With HR Seismic Sources

Following the approach described above, we perform the analysis to a more comprehensive data set composed of 616 thermocline profiles, collected with a depth sampling of 1 m. The associated MSAs have been processed as described in section 4.4 (Figure 12a): in particular the bias error induced by the sampling procedure of the low resolution CTD data set is taken into account as a first approximation to assess the seismic detectability issue.

Similarly to Figure 14a, we first investigate the thermocline detectability of a particular experiment, which is here the synthetic experiment associated to a peak frequency  $F_p = 180$  Hz analyzed in the whole SEC range 109–129 dB of the HR domain. The detectability increases with the SEC parameter: in the worst seismic experiment conditions of a low seismic strength, a low fold, and a high ambient noise level, the minimum detectability is about 55%, which highlights the efficiency of HR seismic systems in detecting seasonal thermoclines. For SEC values higher than 120 dB, the detectability stabilizes about 90%, which represents the amount of thermoclines deeper than the minimum depth of 25 m imposed by the source signature (see section 5.3).

We also highlight the effect of both the ambient noise and fold parameters on the detectability assessed from the HR Synthetic experiment (Figure 15b). As expected, multichannel data acquisitions are required to promote the detection of weak seasonal thermoclines, in particular to face the limitation of a high noise level (blue curve): when no thermocline can be detected for monochannel experiments, more than 80% of the thermoclines can be detected as far as the fold gets larger than 80, which is not that high for actual multichannel seismic experiments. Note that for seismic experiments performed with a low ambient noise level (red curve), a fold parameter greater than 20 does not strongly improve the capacity of the seismic experiment in detecting thermoclines. As a result, a multichannel acquisition with a fold of 100 appears as a sufficient and necessary condition to improve the detection of seasonal thermoclines for any noisy conditions of acquisition.

The approach is finally performed for the whole frequency range 50–300 Hz of the HR domain (Figure 15c). At low frequencies, when the MSA are maximum (Figure 12a), the detectability is close to zero because of the long duration of the seismic signature: for instance, a seismic frequency of 50 Hz can image thermoclines deeper than 90 m, which is not satisfied by most of the shallow seasonal thermoclines of the Armorican shelf. This highlights the limits of low frequencies in detecting thermoclines. On the contrary, higher frequencies do not suffer from depth limitation on the thermocline location and can reach 90% of detectability when considering both  $F_p > 200$  Hz and  $SEC > 120$  dB. Seismic experiments designed in the HR domain are thus perfectly adapted to detect seasonal thermoclines, but they cannot be used to assess the fine-scale structure of such weak shallow reflectors.

It is interesting to note here that the boundary  $F_p = 300$  Hz and  $SEC = 110$  dB is in common for both the HR and VHR analysis: the former, based on a more comprehensive data set, indicates a detectability of 42% in agreement with the detectability based on the latter. This highlights the continuity between the HR and VHR domains analyzed in the present analysis.

## 7. Concluding Remarks

We provide a first statistical description of the frequency dependence and range of variability of the seismic reflection amplitude of the midlatitude Ocean Surface Boundary Layer (OSBL) base, using a data set of CTD profiles collected on the Armorican Shelf by profiling floats of the ARGO network: this study highlights that the seismic amplitude can be approximated by a normal distribution of standard deviation 5.5 dB, centered on  $-14.8 \log(f) - 73.4$  dB, where  $f$  stands for the seismic peak frequency ranging in 50–1000 Hz. We show that collecting the hydrographic profiles with a bin-averaged 1 dbar resolution such as widely available in the oceanographic community leads to an amplitude underestimation which can be reduced by replacing bin-averaging by a properly anti-aliased undersampling of the raw CTD measurements. We put in evidence

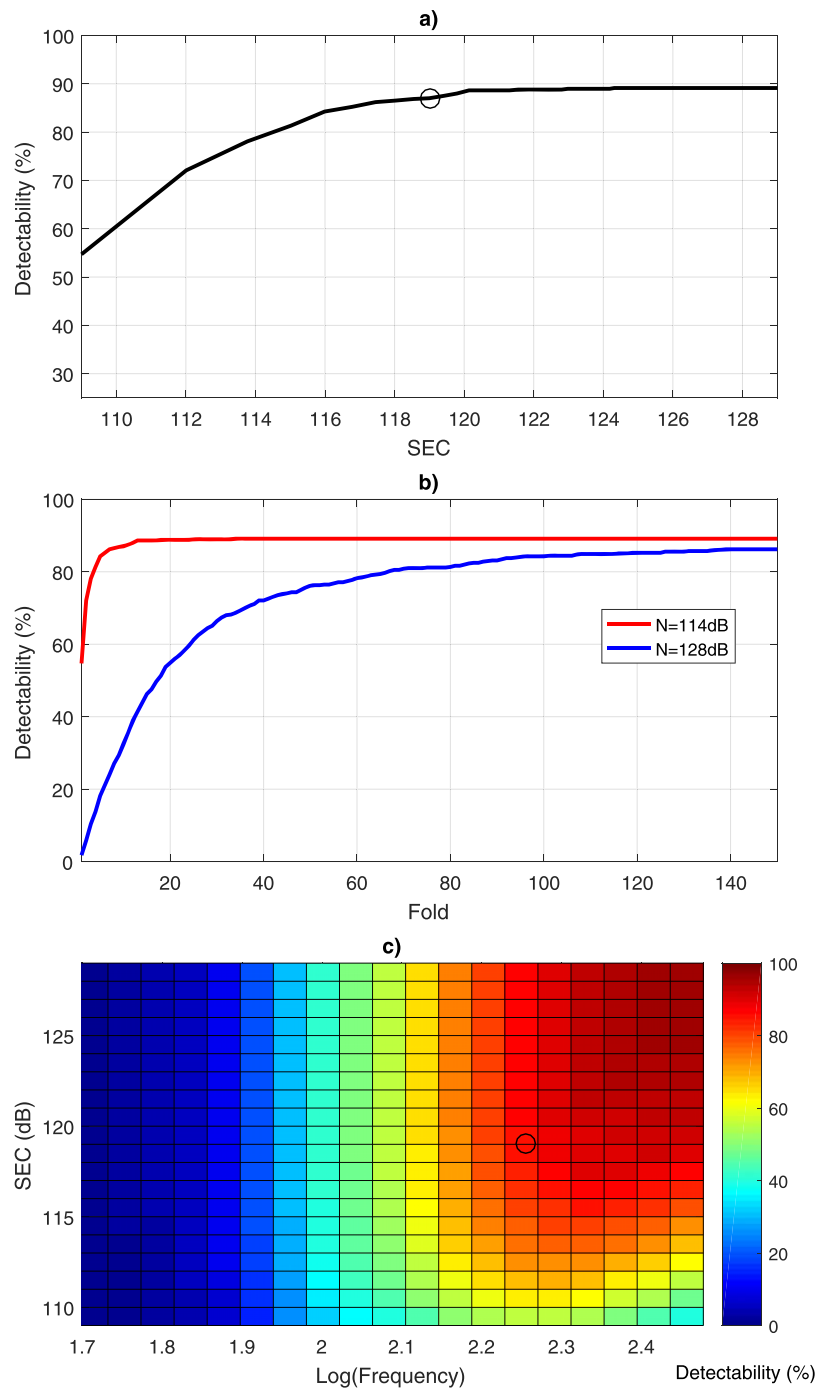


**Figure 15.** (a) Detectability determined from the MSA data set at the peak frequency  $F_p = 180$  Hz as a function of the SEC parameter. The circle indicates the synthetic airgun experiment (see Table 2). (b) Detectability of the HR experiment for a low (red) and high (blue) level of noise plotted as a function of the fold parameter. (c) Detectability determined in the SEC range 109–129 dB and peak frequency range 50–300 Hz associated to the HR domain.

that fitting a simple Gauss Error Function to the dominant temperature contrast, while useful as a conceptual tool [Ker et al., 2015], is not a sufficiently robust way to estimate the frequency-dependent OSBL base seismic reflectivity, for instance in the planning stage of a seismic oceanography experiment. This statistical characterization allows us discussing, in a broader context, the ASPEX seismic observations of the OSBL base which seismic amplitude is at least 10 dB higher than the 98th percentile of all the amplitudes performed with the data set: the ASPEX thermocline was in fact very exceptional in its sharpness and a

tentative explanation is that the seismic observations were performed a very short time after a strong mixing event due to the passage of a storm.

We introduced the Seismic Experiment Capability (SEC), a new parameter used to define the global capability of a seismic experiment to detect a thermocline, accounting for the seismic source strength, the processing chain and the ambient noise level: the study can be extended both to the frequency range 50–1000 Hz and to the large SEC range 90–129 dB, covering different configurations of seismic experiments. This allows assessing the seismic detectability of shallow seasonal thermoclines and stating a few recommendations for the design of seismic experiments better suited to the study of the thermohaline structure of the OSBL. A high SEC value is always recommended, which requires a high source strength, a high fold acquisition and a low ambient noise level. From the study, a fold of 100 appears necessary to improve the detection of seasonal thermoclines for any noisy conditions of acquisition. Moreover, the decrease of seismic amplitude with increasing frequency seems to indicate the use of low-frequency sources: in the meantime, shallow oceanic reflectors cannot be imaged by the use of long-duration seismic signatures and we show that it is possible to reach a detectability of 90% when considering both  $400 \text{ Hz} > f > 200 \text{ Hz}$  and  $\text{SEC} > 120 \text{ dB}$ . Current-day sources, i.e., airguns, emit parasitic signals which make them ill-suited to the study of shallow reflectors [Piété *et al.*, 2013]: the chirp source proposed by Biescas *et al.* [2016] might provide a satisfactory alternative but significant technological advances are still required to be able to emit powerful chirp signals in this high-frequency range. Such improvements can lead to detect most of the seasonal thermocline profiles present in our database with the seismic technique, and could make seismic oceanography a suitable tele-detection technique for the study of the OSBL thermohaline complex structure.

#### Acknowledgments

It is a pleasure to thank Y. Thomas and B. Marsset for providing seismic signatures of ASPEX and IFOSISMO experiments and for stimulating discussions, H. Piété who contributes to the acquisition and analysis of the ASPEX data set, M.-A. Gütscher for giving access to the IFOSISMO dataset, and two anonymous reviewers for their comments which contribute to improve the paper. The Argo data were collected and made freely available by the International Argo Program and the national programs that contribute to it (<http://www.argo.ucsd.edu>). The Argo Program is part of the Global Ocean Observing System.

#### References

- André, X., S. Le Reste, and J.-F. Rolin (2010), ARVOR-C, a coastal autonomous profiling float, *Sea Technol.*, *51*, 10–13.
- Batifoulie, F., P. Lazure, L. Velo-Suarez, D. Maurer, P. Bonneton, G. Charria, C. Dupuy, and P. Gentien (2013), Distribution of *Dinophysis* species in the Bay of Biscay and possible transport pathways to Arcachon Bay, *J. Mar. Syst.*, *109*, S273–S283.
- Biescas, B., V. Sallarès, J.-L. Pelegrí, F. Machín, R. Carbonell, G. Buffett, J.-J. Dañobeitia, and A. Calahorrano (2008), Imaging Meddy fine structure using multichannel seismic reflection data, *Geophys. Res. Lett.*, *35*, L11609, doi:10.1029/2008GL033971.
- Biescas, B., L. Armi, V. Sallarès, and E. Gràcia (2010), Seismic imaging of staircase layers below the mediterranean undercurrent, *Deep Sea Res., Part 1*, *57*, 1345–1353.
- Biescas, B., N. Ruddick, J. Kormann, V. Sallarès, M. R. Nedimović, and S. Carniel (2016), Synthetic modeling for an acoustic exploration system for physical oceanography, *J. Atmos. Oceanic Technol.*, *33*, 191–200.
- Boccaletti, G., R. Ferrari, and B. Fox-Kemper (2007), Mixed layer instabilities and restratification, *J. Phys. Oceanogr.*, *37*, 2228–2250.
- Brown, J., K. Brander, L. Fernand, and A. E. Hill (1996), Scanfish: High performance towed undulator, *Sea Technol.*, *37*, 23–27.
- Buffett G.G., B. Biescas, J. L. Pelegrí, F. Machin, V. Sallarès, R. Carbonell, D. Klaeschen, and R. Hobbs (2009), Seismic reflection along the path of the Mediterranean Undercurrent, *Cont. Shelf Res.*, *29*, 1848–1860.
- Chapman, N. R., and A. Price (2011), Low frequency deep ocean ambient noise in the Northeast Pacific Ocean, *J. Acoust. Soc. Am.*, *129*, 161–165.
- Charria, G., P. Lazure, B. Le Cann, A. Serpette, G. Reverdin, S. Louazel, F. Batifoulie, F. Dumas, A. Pichon, and Y. Morel (2013), Surface layer circulation derived from Lagrangian drifters in the Bay of Biscay, *J. Mar. Syst.*, *109–110*, S60–S76.
- de Boyer Montégut, C., G. Madec, A. Fischer, A. Lazar, D. Iudicone (2004), Mixed layer depth over the global ocean: An examination of profile data and a profile-based climatology, *J. Geophys. Res.*, *109*, C12003, doi:10.1029/2004JC002378.
- Ferrari, R. (2011), A frontal challenge for climate models, *Science*, *332*, 316–317.
- Fer, I., P. Nandi, W. Holbrook, R. Schmitt, and P. Pàramo (2010), Seismic imaging of a thermohaline staircase in the western tropical north Atlantic, *Ocean Sci.*, *6*, 621–631.
- Géli, L., E. Cosquer, R. W. Hobbs, D. Klaeschen, C. Papenberg, Y. Thomas, C. Menesguen, and B. L. Hua (2009), High resolution seismic imaging of the ocean structure using a small volume airgun source array in the Gulf of Cadiz, *Geophys. Res. Lett.*, *36*, L00D09, doi:10.1029/2009GL040820.
- Goupillaud, P. (1961), An approach to inverse filtering of near-surface layer effects from seismic records, *Geophysics*, *26*, 754–760.
- Gula, J., M. J. Molemaker, and J. C. McWilliams (2015), Topographic vorticity generation, submesoscale instability and vortex street formation in the Gulf Stream, *Geophys. Res. Lett.*, *42*, 4054–4062, doi:10.1002/2015GL063731.
- Hobbs, R. W., D. Klaeschen, V. Sallarès, E. Vsemirnova, and C. Papenberg (2009), Effect of seismic source bandwidth on reflection sections to image water structure, *Geophys. Res. Lett.*, *36*, L00D08, doi:10.1029/2009GL040215.
- Holbrook, W. S., and I. Fer (2005), Ocean internal wave spectra inferred from seismic reflection transects, *Geophys. Res. Lett.*, *32*, L15606, doi:10.1029/2005GL023733.
- Holbrook, W. S., P. Pàramo, S. Pearse, and R. Schmitt (2003), Thermohaline fine structure in an oceanographic front from seismic reflection profiling, *Science*, *301*, 821–824.
- Holbrook, W. S., I. Fer, and R. Schmitt (2009), Images of internal tides near the Norwegian continental slope, *Geophys. Res. Lett.*, *36*, L00D10, doi:10.1029/2009GL038909.
- Johnston, T. M. S., and D. L. Rudnick (2009), Observations of the transition layer, *J. Phys. Oceanogr.*, *39*, 780–797.
- Ker, S., Y. Le Gonidec, D. Gibert, and B. Marsset (2011), Multiscale seismic attributes: A wavelet-based method and its application to high-resolution seismic and ground truth data, *Geophys. J. Int.*, *187*, 1038–1054.
- Ker, S., Y. Le Gonidec, and D. Gibert (2012), Multiscale seismic attributes: Source-corrected wavelet response and its application to high-resolution seismic data, *Geophys. J. Int.*, *190*, 1746–1760.

- Ker, S., Y. Le Gonidec, L. Marié, Y. Thomas, and D. Gibert (2015), Multiscale seismic reflectivity of shallow thermoclines, *J. Geophys. Res. Oceans*, *120*, 1872–1886, doi:10.1002/2014JC010478.
- Kersalé, M., L. Marié, B. Le Cann, A. Serpette, C. Lathuilire, A. Le Boyer, A. Rubio, and P. Lazure (2016), Poleward along-shore current pulses on the inner shelf of the Bay of Biscay, *Estuarine Coastal Shelf Sea*, *179*, 155–171, doi:10.1016/j.ecss.2015.11.018.
- Koutsikopoulos, C., and B. Le Cann (1996), Physical processes and hydrological structures related to the Bay of Biscay anchovy, *Sci. Mar.*, *60*(Supl. 2), 9–19.
- Landrø, M. (1992), Modelling of GI gun signatures, *Geophys. Prospect.*, *40*, 721–747.
- Laws R. M., L. Hatton, and M. Haartsen (1990), Computer modeling of clustered air gun, *First Break*, *8*, 331–338.
- Le Boyer, A., G. Charria, B. Le Cann, P. Lazure, and L. Marié (2013), Circulation on the shelf and the upper slope of the Bay of Biscay, *J. Mar. Syst.*, *109*, S134–S143.
- Le Gonidec, Y., D. Gibert, and J.-N. Proust (2002), Multiscale analysis of waves reflected by complex interfaces: Basic principles and experiments, *J. Geophys. Res.*, *107*(B9), 2184, doi:10.1029/2001JB000558.
- Lévy, M., P. Klein, A.-M. Tréguier, D. Iovino, G. Madec, S. Masson, and K. Takahashi (2010), Modifications of gyre circulation by sub-mesoscale physics, *Ocean Modell.*, *34*, 1–15.
- Lurton, X. (2002), *An Introduction to Underwater Acoustics: Principles and Applications*, Springer, London, U. K.
- Mallat, S. (1998), *A Wavelet Tour of Signal Processing*, 2nd ed., Academic, Burlington, Vermont.
- Mallat, S., and W. L. Hwang (1992), Singularity detection and processing with wavelets, *IEEE Trans. Inf. Theory*, *38*, 617–643.
- Ménesguen, C., B. Hua, X. Carton, F. Klingelhoefer, P. Schnurle, and C. Reichert (2012), Arms winding around a Meddy seen in seismic reflection data close to the morocco coastline, *Geophys. Res. Lett.*, *39*, L05604, doi:10.1029/2011GL050798.
- Millero, F. J., C. Chen, A. Bradshaw, and K. Schleicher (1980), A new high pressure equation of state for seawater, *Deep Sea Res. Part A*, *27*, 255–264.
- Mirshak, R., M. R. Nedimovic, B. J. W. Greenan, B. Ruddick, and K. Loudon (2010), Coincident reflection images of the gulf stream from seismic and hydrographic data, *Geophys. Res. Lett.*, *37*, L05602, doi:10.1029/2009GL042359.
- Perrone, A. J. (1969), Deep-ocean ambient-noise spectra in the northwest Atlantic, *J. Acoust. Soc. Am.*, *46*(3B), 762–770.
- Piété, H., L. Marié, B. Marsset, Y. Thomas, and M.-A. Gutscher (2013), Seismic reflection imaging of shallow oceanographic structures, *J. Geophys. Res. Oceans*, *118*, 2329–2344, doi:10.1002/jgrc.20156.
- Pingree, R. D., and A. L. New (1995), Structure, seasonal development and sunglint spatial coherence of the internal tide on the Celtic and Armorican shelves and in the Bay of Biscay, *Deep-Sea Res. Part. I*, *42*, 245–284.
- Ponté, A. L., P. Klein, X. Capet, P.-Y. Le Traon, B. Chapron, and P. Lherminier (2013), Diagnosing surface mixed layer dynamics from high-resolution satellite observations: Numerical insights, *J. Phys. Oceanogr.*, *43*, 1345–1355.
- Puillat, I., P. Lazure, A.-M. Jégou, L. Lampert, and P. I. Miller (2004), Hydrographic variability on the French continental shelf in the Bay of Biscay during the 1990s, *Cont. Shelf Res.*, *25*, 1143–1163.
- Reverdin, G., et al. (2013), Freshwater from the Bay of Biscay shelves in 2009, *J. Mar. Syst.*, *109–110*, S134–S143.
- Riser, S. C., et al. (2016), Fifteen years of ocean observations with the global Argo array, *Nat. Clim. Change*, *6*, 145–153.
- Ruddick, B., H. B. Song, C. Z. Dong, and L. Pinheiro (2009), Water column seismic images as maps of temperature gradient, *Oceanography* *22*, 192–205.
- Sallarès, V., B. Biescas, G. Buffett, R. Carbonell, J. J. Dañobeitia, and J. L. Pelegrí (2009), Relative contribution of temperature and salinity to ocean acoustic reflectivity, *Geophys. Res. Lett.*, *36*, L00D06, doi:10.1029/2009GL040187.
- Sallarès, V., J. F. Mojica, B. Biescas, D. Klaeshen, and E. Gràcia (2016), Characterization of the submesoscale energy cascade in the Alboran Sea thermocline from spectral analysis of high-resolution MCS data, *Geophys. Res. Lett.*, *43*, 6461–6468, doi:10.1002/2016GL069782.
- Somavilla, R., C. González-Pola, A. Lavin, C. Rodriguez (2013), Temperature and salinity variability in the south-eastern corner of the Bay of Biscay (N.E. Atlantic), *J. Mar. Syst.*, *109–110*, S105–S120.
- Thomas, Y., B. Marsset, L. Marié, S. Ker, and H. Piété (2013), Compte rendu de mission: Mission IFOSISMO, N/O Côtes de la Manche 20-23 septembre 2012. Adéquation de la source sismique sparker à l'imagerie de la thermocline en mer d'Iroise., technical report, PDG/REM/GM/EIS-08022013-01, IFREMER, Brest.
- Urick, R.J. (1983), *Principles of Underwater Sound*, 422 pp., Mc Graw-Hill, N. Y.
- Vincent, A. (1973), Les variations de la situation thermique dans le Golfe de Gascogne en 1969 et 1970, *Rev. Trav. Inst. Pches Marit.*, *37*, 5–18.
- Wang, Y. (2015), The Ricker wavelet and the Lambert W function, *Geophys. J. Int.*, *200*, 111–115.
- Wenz, G. M. (1962), Acoustic ambient noise in the Ocean: Spectra and sources, *J. Acoust. Soc. Am.*, *34*(12), 1936–1956.
- Yilmaz, O. (1987), *Seismic Data Processing*, Soc. of Explor. Geophys., Tulsa, Okla.
- Ziolkowski A, G. Parkes, L. Hatton, and T. Haugland (1982), The signature of an air gun array: Computing from near-field measurement including interactions, *Geophysics*, *47*, 1413–1421.